Optical Measurement of Propeller Blade Deflections

Anatole P. Kurkov

Optical Measurement of Propeller Blade Deflections

Anatole P. Kurkov
Lewis Research Center
Cleveland, Ohio

Summary

A nonintrusive optical method for measuring propeller blade deflections is described and evaluated. The measurement does not depend on blade surface reflectivity. Deflection of a point at the leading edge and a point at the trailing edge in a plane nearly perpendicular to the pitch axis is obtained with a single light beam generated by a low-power, helium-neon laser. Quantitative analyses are performed from taped signals on a digital computer. Averaging techniques are employed to reduce random errors. Measured deflections from a static test and a series of high-speed tests are compared with available predicted deflections, which are also used to evaluate systematic errors.

Introduction

This report describes an optical method for measuring blade deflections of turbomachinery rotors. The method is especially well suited for rotors that are tested without engine casings or any other walls next to the blade tips (i.e., for propellers, propfans, and unducted fans). In fact, it complements the already established optical blade deflection method (refs. 1 to 5), which relies on blade tip reflection of the incident light beam and thus requires a close proximity of the casing to the blade tips. The method described in this report can also be used during structural tests of turbomachinery rotors in vacuum spin rig facilities.

In this method a concentrated light beam, such as generated by a laser, is directed to the blade pressure surface in a plane approximately perpendicular to the pitch axis. The incident light beam forms a small angle relative to the chord, usually about 10°. The overall schematic of the experiment is given in figure 1, and the relationship of the beam and the undeflected blade in figure 2. As the blades rotate, the leading and trailing edges intersect the light beam. Therefore, by placing a photodetector in the path of the light beam after it crosses the plane of rotation, one can obtain a series of negative pulses, each associated with the period of time when the light was shadowed from the detector by a blade. If, in addition, a once-per-revolution reference pulse is generated, these pulses can provide an indication of the instantaneous blade positions for each revolution in a rotating frame of reference.

Nonintegral engine-order vibrations, such as flutter, can be quantitatively analyzed with this non-reflected-light system just as described in reference 6 for a reflected-light system.

Detection of integral engine-order vibrations requires the arrangements described in references 1 and 3. These vibrations can also be analyzed quantitatively, as demonstrated in a spin rig facility, by using a multiport optical arrangement, with each port having its own microprocessor (ref. 7). This report, however, is confined to quantitative determination of static blade deflections for propellers and unducted fans by using a single laser beam per blade span.

Although dynamic stress data for propellers have been collected over the years by means of strain gages, direct measurements of static deflections have seldom been available. Typically, either strobe photographs of blade tips (refs. 8 to 10) or line-of-sight transit measurements during the run (ref. 11) have been employed for nonintrusive measurements. Intrusive measurements have been made by mounting small mirrors on the blade surface (refs. 9, 10, and 12). These measurements also relied on photographic records.

In the present method all quantitative analyses are performed from the taped signals on a minicomputer. Thus averaging in time and space can be easily incorporated to reduce random errors. Moreover, the method depends not on the reflectivity of the blade surface but only on its opaqueness and is completely nonintrusive. Note also that, unlike in the reflected-light method, here one light beam essentially measures the deflection of two points, one at the leading edge and one at the trailing edge, for any particular blade span.

Experimental data from two tests illustrate the use of the method. One is a static (i.e., zero free-stream air velocity)
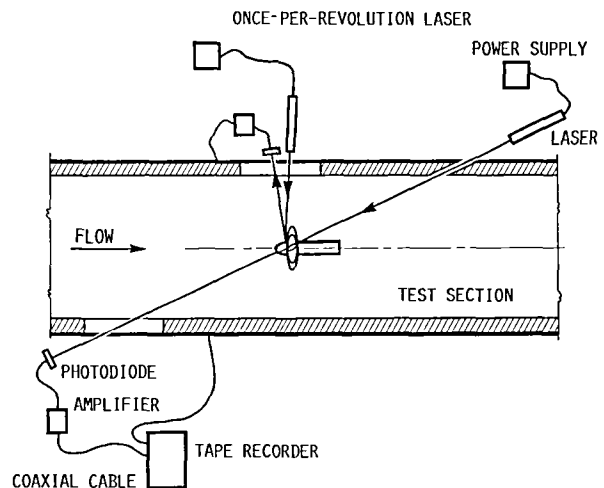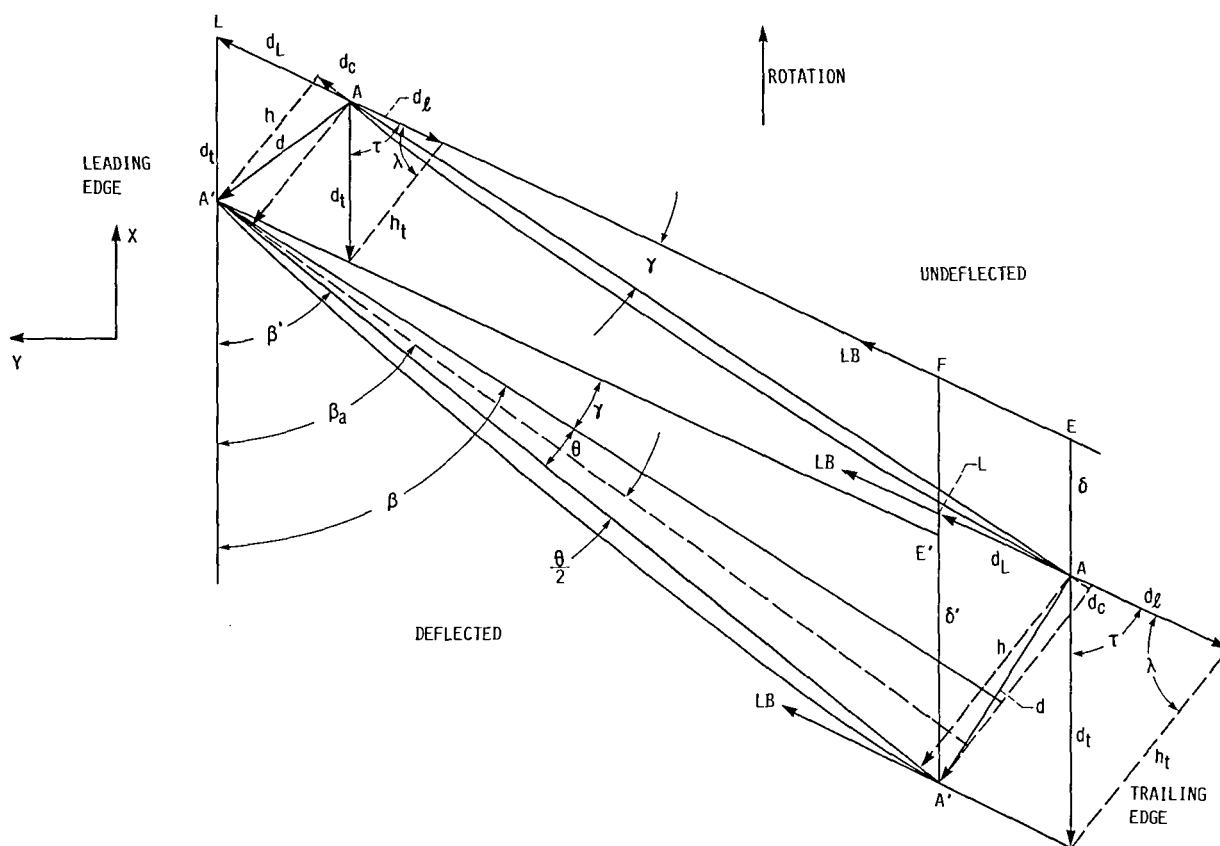

Figure 1.—Test schematic.

Figure 2.—Laser beam and blade section geometry.

test of a 2.74-m propeller built by the Hamilton Standard Division of the United Technologies Corporation, and the other is the high-speed test of a series of 0.61-m model rotors incorporated in a counterrotating, unducted-fan arrangement built by the General Electric Company. The static test was performed in the Wright-Patterson Air Force Base (WPAFB) test facility (fig. 3), and the high-speed test was performed in the Lewis Research Center's 8- by 6-ft (2.44 by 1.83 m) wind tunnel (fig. 4). Some of the optical hardware used in the test can be seen in figure 3 on the far wall and behind the window in figure 4. A plan view of the blades tested is given in figure 5. All the blades had a composite shell. The report also includes predicted deflections obtained from aerostructural finite-element code outputs supplied by the respective manufacturers. Additional information on the SR–7L and F7 blades and their performance is available in references 13 and 14, respectively.

For the purpose of comparing experimental and predicted deflections, one can always calculate the particular deflection component that is being measured. (Note that throughout the report, deflections derived from the supplied aerostructural finite-element code outputs are referred to as predicted deflections.) However, because in the present case the measured component is not a generally accepted or easily defined quantity and because it could easily be misinterpreted, the more commonly accepted deflection parameters such as

bending and twist deflections are derived from experimental measurements and compared with predictions. Both of these deflections can be obtained from measurements because they depend on the displacement perpendicular to the chord and the light beam makes only a small angle relative to the chord. The errors associated with these estimates are largely caused by the finite incidence angle of the laser beam relative to the blade and the fact that the sensor (i.e., the laser beam–detector combination) is fixed in space, and not with respect to the blade, as is a strain gage, for example. The net effect is that a blade edge is free to slip relative to the laser beam during blade deformation. Because these errors are inherent in the experimental procedure, they can be classified as systematic, or bias, errors.

The measured twist and bending deflections can only be relied upon if these errors are small. Systematic errors are estimated by cutting the finite-element, deflected-blade contour by a line coincident with the laser beam in the same way the real deflected blade is cut by a laser beam during the test. Since in this case the true displacements of the original contact points between the undeflected blade and the laser beam are also known, the incidence and the slip effects can be evaluated.

Note that, when equations that assume the exact knowledge of the deflected-blade shape are presented in the report, it is to illustrate where the measured deflections fall short of the true deflections and eventually to estimate systematic errors.
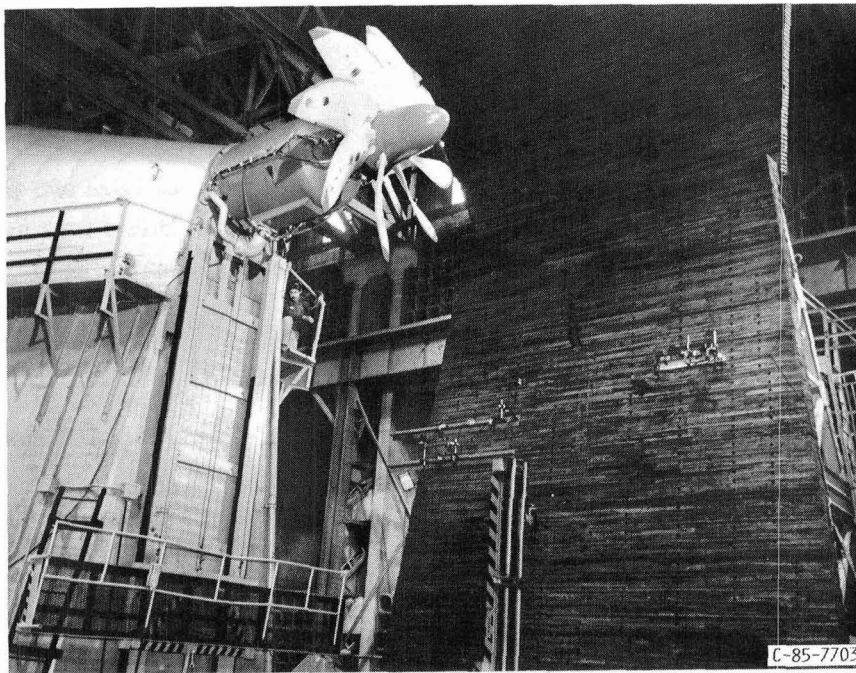
Figure 3.—SR–7L propeller in Wright-Patterson Air Force Base static test facility.
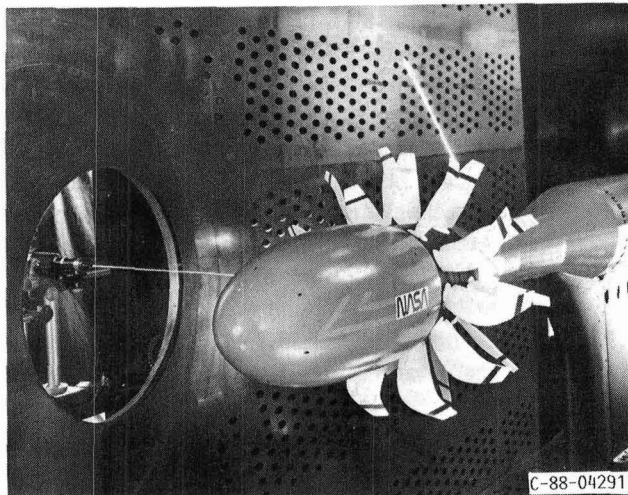
Figure 4.—Counterrotating propeller and helium-neon lasers installed in Lewis 8- by 6-ft wind tunnel.

(a) Static test.
(b) High-speed tests.

Figure 5.—Blade schematics—plan view.

Only the undeflected-blade, finite-element contour is used for defining the initial geometric conditions for measured deflections.

Because only incomplete information was available for the F21 blade, the systematic-error analysis for this blade could not be completed. For this reason the F21 results are presented separately in the next-to-last part of the "Results" section. Although there appears to be a distinction in the current literature between unducted fans, propfans, and propellers, all rotors in this report are referred to, for simplicity, as propellers. The essential similarity from the instrumentation point of view is that these rotors are not encased.

Symbols

a_y, a_z	slopes defined by eqs. (3) and (4)
b_y, b_z	constants (eqs. (3) and (4))
C	chord (eq. (16))
$C_{\theta/2}$	defined by eq. (72)
c_x, c_z	slopes defined by eqs. (5) and (6)
d	displacement (fig. 2)
d_c, d_ℓ	displacements (fig. 2, eqs. (25) and (26))
d_t, d_L	displacements (fig. 2, eq. (24))

d_x, d_z	constants (eqs. (5) and (6))
h	displacement component normal to chord (fig. 2, eq. (25))
h_p, h_{tp}	h, h_t projected on plane normal to $\hat{n}_h$
h_t	component d_t normal to chord (fig. 2, eq. (26))
i,j,k	associated with Cartesian unit vectors
N_f	fraction of design speed
n_c	associated with unit vector given by eq. (66)
n_{ch}	associated with unit vector given by eq. (49)
$n_{c\ell}$	associated with unit vector given by eq. (67)
n_h	associated with unit vector given by eq. (54)
n_t	associated with unit vector given by eq. (63)
$n_{t\ell}$	associated with unit vector given by eq. (60)
P,Q	coefficients (eqs. (10) to (12))
R	polar cylindrical coordinate (eq. (7))
r	radius associated with point vector
S_h	sign function given by eq. (48)
S_t	sign function given by eq. (59)
t_{cn}	defined by eq. (71)
V_ℓ	defined by eq. (17)
X,Y,Z	Cartesian coordinates (fig. 2); Y coincident with rotational axis and Z with pitch axis
α	angle defined by eqs. (1) and (2)
β	blade angle (fig. 2)
γ	beam incidence angle (fig. 2)
δ	defined in fig. 2 and eq. (14)
δ_{ta}	defined by eq. (53)
δ_y	axial deflection (eq. (82))
θ	twist angle (fig. 2)
λ, τ	defined in fig. 2 and eq. (27)
φ	polar cylindrical coordinate (eq. (7))
$\varphi_t, \varphi_{t/2}$	defined by eqs. (20), (22), and (58)
$\varphi_\delta, \varphi_{\delta/2}$	defined by eqs. (12) and (15)

Subscripts:

A	denotes a point in fig. 2
a	denotes average
E,F,L	denote points in fig. 2
LE,TE	denote leading and trailing edges
k	relates to XY plane
ℓ	denotes laser beam
n	relates to plane nominal to n (can be subscripted)
nom	nominal
s	denotes finite-element edge segment

Special symbols:

S	vector associated with segment S
$\hat{S}$	unit vector associated with S
S'	deflected value of S
$\bar{S}$	true predicted value of S (no-slip condition)
$\tilde{S}$	value of S derived from measurements
S''	predicted value of S using C = Constant assumption

Experimental Measurements

Geometry of Laser Beam and Blade

Figure 2 shows the deflected and undeflected blade sections obtained by cutting the respective blades with a laser beam that is nearly perpendicular to the pitch axis. The coordinate system is fixed with respect to the blade. The Y axis is coincident with the rotational axis, and the Z axis is coincident with the blade pitch axis and points upward. Lines that are either in the direction of the average chord line or are perpendicular to it are shown as dashed lines for ease of recognition.

In the experiment the laser beam is fixed in space and the blades are rotating. As a blade is deflected it will intersect the laser beam somewhat earlier or later than the undeflected blade, measured relative to the occurrence of the once-per-revolution signal. In figure 2, however, the blades are assumed to be stationary, and the laser beam is assumed to be rotating opposite to the direction of rotation. Thus, to get the laser beam to be tangent to the deflected blade contour at the leading edge, one must rotate the laser beam until points L (assumed to be fixed relative to the laser beam) and A' coincide. The referred lag or advance times (measured relative to the once-per-revolution signal) translate in figure 2 as the leading- or trailing-edge tangential displacements d_t. Rotating the beam rather than the blades allows one to keep the same coordinate system for the deflected and undeflected blades, just as in a typical aerostructural finite-element code.

In the test the data for the undeflected blades were collected at some reference speed sufficiently low for blade deflections to be negligible, and the deflected-blade data usually corresponded to a speed near the design value for a given Mach number.

Experimental Equipment

Low-power, helium-neon lasers were selected for this experiment because of their low cost and rugged, compact construction and because they provide a monochromatic source of light. The minimum power rating for the lasers was 1 mW, which was sufficiently low to allow safe operation without imposing special operating restrictions. Large-area silicon photodiodes manufactured by United Detector Technology (UDT) were selected for the detectors.

This basic system, consisting of a laser and a photodiode, was enhanced by using a commercial beam expander to focus the laser beam onto a blade and by using an optical line filter to shield the extraneous light from the detector. In addition, the effective receptor area was enlarged by placing a simple biconvex lens, twice the diameter of the detector, about half its focal length in front of the detector. Positioning the detector away from the focal point protected it from concentrated light.

The focused beam diameters in the plane of rotation were about 3 mm for the static test and about 1.5 mm for the wind tunnel tests (fig. 1). Typical distances crossed by a laser beam were 5 m for the wind tunnel tests and 25 m for the static test. Therefore, photodiodes with active diameters of 12 and 28 mm were selected for the wind tunnel tests and the static test, respectively. Typical rise times (as reported by the manufacturer) were 10 ns for the smaller and 50 ns for the larger photodiode. Model 201A (UDT) amplifier was used to provide the bias current for the photodiode and to convert the photodiode output to a suitable voltage that could be transmitted to the tape recorder. The frequency responses of this amplifier and the wideband II frequency-modulated (FM) tape recorder were both 0.5 MHz.

In addition to the blade signals it was also necessary to generate a once-per-revolution signal of the same quality. This was achieved by attaching a small mirror to the hub of a propeller and reflecting the nearly perpendicular incident laser beam onto a photodiode detector placed (at the time of reflection) opposite the mirror.

Rigid, manually adjustable and lockable optical holders and bases were used to align and secure the lasers and the detectors. Although this equipment made the alignment process somewhat tedious, it ensured that lasers and detectors were not thrown out of alignment by the severe vibratory environment during the tests. For assurance that optical alignment was not changed during a run, alignment checks were made before and after each test run.

Laser Beam Alignment

For the static test of the large-scale propeller, laser beams were located in the plane nearly perpendicular to the pitch axis at each spanwise station. The spanwise stations were marked on a particular blade as lines normal to the pitch axis. This blade was rotated before the test so that it was approximately in the six o'clock position and the lines denoting measurement stations were horizontal.

Positions of lasers on the test section walls were determined by the requirements that each beam mark a spot at about midchord of a measurement station on a blade and that it make a predetermined incidence angle γ relative to the blade chord in the horizontal plane. Because the suction-side contour was more convex, the laser beams were always aimed to trace the blade pressure side. For each measurement station lasers were placed on the walls either behind the plane of rotation (the region of negative Y in fig. 2) or in front, depending on the spanwise station and the blade setting angle. This was

necessary because only a limited length of the test section walls was suitable for mounting optical hardware. When a laser is behind the plane of rotation, the angle that the beam makes with the wall (i.e., the Y axis) is

$$\alpha = 90 - (\beta + \gamma) \tag{1}$$

and when a laser is in front of the rotational plane, it is

$$\alpha = 90 - (\beta - \gamma) \tag{2}$$

The analysis is presented only for the former case, which is shown in figure 2, since for the latter it can always be reconstructed following the procedure presented in this report. The incidence angle γ was typically 10°. After the lasers were aligned relative to the blades, the detectors were placed on the opposite wall of the test section so that the beams were centered and normal to their surface.

Note that the initial beam orientation relative to the undeflected blade for these tests is not as shown in figure 2 (since the laser beam was directed to the blade midchord at each span). However, the measured angle α of the laser beam relative to the Y axis, the known angle β, the Z coordinate at each measuring station, and the fact that the beam intersected a blade at the midchord provided sufficient information to determine the coordinates of points A. After these coordinates had been determined, the laser beam was rotated until it was tangent to the leading edge of the undeflected blade, as shown in figure 2.

Figure 2, on the other hand, correctly describes the initial arrangement for the high-speed tests in the wind tunnel. In these tests the model had two counterrotating blade rows. It was necessary therefore to bypass one of the rotors with the beam by tilting the laser slightly toward or away from the axis so that only one blade row intersected the beam. This could be achieved only for the near-tip-span measurement station.

The laser beam entered the test section through one of the boundary layer bleed holes in the tunnel walls and exited through a glass window on the opposite wall. The tunnel bleed holes were inclined 30° relative to the tunnel axis, and the window was somewhat upstream of the forward rotor's plane of rotation and centered on the axis. Thus the beam had to exit the tunnel near the axis in the wall window area and at the same time intersect one of the blade rows near the blade tips (which were downstream of the window). These requirements could be met only by aligning the laser beam relative to a blade that was rotated somewhat away from the vertical (12 o'clock) position. This made it more difficult to determine orientation of the plane normal to the pitch axis. (Recall that this plane was chosen for the initial alignment in the static test.) However, one could easily locate the laser beam intercepts at the leading and trailing edges on the alignment blade by rotating this blade slightly and observing the trace of the beam on the blade.

The boundary layer bleed hole through which the laser beam entered the tunnel was therefore selected so that the following requirements were met as closely as possible: (1) the trace of the beam on the pressure surface of a blade was coincident with a marked line perpendicular to the pitch axis; (2) the incidence on the blade was less than 12° and at the same time sufficiently high so that the beam was either cut or uncovered only by the blade edges and required only a small rotation to complete the intersection; (3) the beam tilt relative to the axis was sufficient to pass the beam past one of the blade rows and at the same time have it incident on the upstream window area.

Note that in this report only the data for the forward rotor are presented. For it, the tilt direction required to bypass the aft rotor was toward the axis, the same direction required by the tunnel window.

The laser beam intercepts on the leading and trailing edges were determined indirectly by measuring the distance between the blade tip corners and the trace of the beam on the blade in the direction perpendicular to blade tip. In addition, the incidence angle γ between the chord and the laser beam and the length of the trace (distance AA in fig. 2) were measured directly.

Given the contour of the undeflected blade in the form used by a finite-element code and the two measured intercepts that locate line AA on a blade, coordinates of points A_{LE} and A_{TE} near the tip could be calculated with sufficient accuracy by using planar geometry. From these coordinates chord vector $A_{TE}A_{LE}$ and radii $(R_A)_{LE}$ and $(R_A)_{TE}$ were computed.

From the angle γ, the distance AA, and the fact that the direction of vector δ is that of the tangent to the arc $A_{TE}E$ halfway between points A_{TE} and E, the angle β was computed by using an iterative procedure. The unit vector $\hat{V}_\ell$ that describes the direction of the laser beam was then obtained by using the triangle AAE in figure 2.

This provided sufficient information to begin computing deflections, as described later in the section "Planar Geometry," without resort to the more general three-dimensional procedure described later in the report. However, the three-dimensional formulation of laser beam–blade intersection was still needed to define deflected-blade parameters so that predicted and experimental deflections could be compared. Thus this procedure was applied for the reference conditions (i.e.,

undeflected blade geometry) in the static test and for the design conditions in both the static and high-speed tests.

Experimental Data Reduction

Prerecorded signals from the magnetic tape were processed on a system consisting of a minicomputer, an eight-channel digitizer, and high-volume disk storage peripherals. In the preliminary evaluation it was determined that about 12 000 points per revolution provided sufficient resolution for the recorded signals.

The maximum overall digitizing rate to the disk was about 150 kHz; but, since four channels were usually digitized simultaneously, the maximum rate per channel was one quarter of the overall rate. Extended computer memory was used to provide a sufficiently large buffer for data during the digitization.

The playback speed was selected so that the maximum rate per channel was not exceeded when meeting the requirement for the desired number of points per revolution. Depending on the rotational speed and the number of channels selected for simultaneous digitization, the playback speed ranged from 1⅞ to 15 in./s (4.76 to 38.1 cm/s). (Note that the recording speed was always 120 in./s (304.8 cm/s).)

Stored on a magnetic disk were therefore a series of negative-going digital pulses for each blade span and a series of positive-going once-per-revolution digital pulses corresponding to the signals reflected from the hub mirror. An example of each pulse is given in figures 6 and 7.

The first negative drop in voltage for a blade pulse corresponds to a progressive blockage of the laser light reaching the detector by the blade leading edge. The subsequent rise in voltage corresponds to the uncovering of the laser beam by the trailing edge. Therefore, by selecting some suitable voltage near the steepest slopes region to define a blade-pulse trigger, one can associate the corresponding times with the instantaneous blade leading- and trailing-edge positions for a particular blade section as determined by the geometry of the blade and the laser beam.

The once-per-revolution pulse subdivides the continuous blade-pulse train into consecutive revolutions. From this, one can obtain the shaft rotational speed and then express the
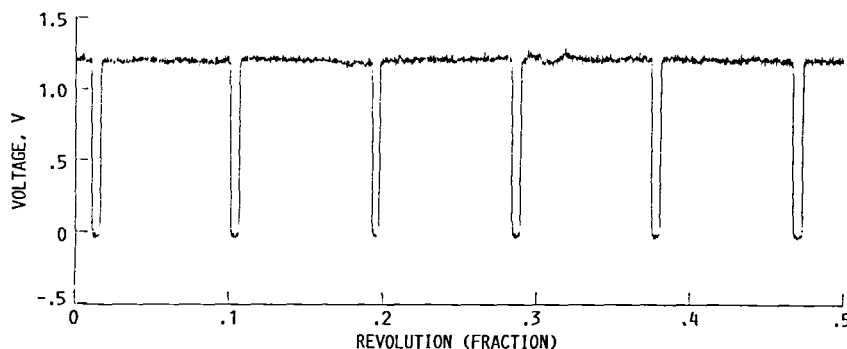

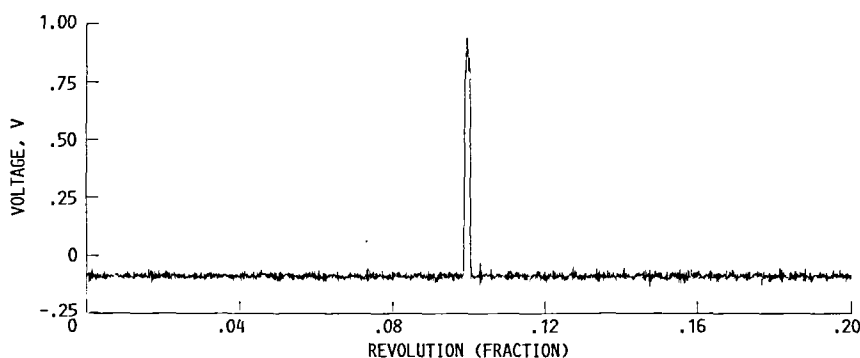Figure 6.—Blade tip pulses—F11 blade.

Figure 7.—Once-per-revolution pulse—F11 hub.

position of each blade pulse in terms of a relative angular coordinate in the plane of rotation. These blade positions are typically averaged over about 50 revolutions.

The outlined procedure was applied to the data associated with some low reference speed, where blade deflections were very small and consequently could be neglected, and to the data associated with some higher speed, usually near the design speed, where deflections are significant. Subtracting the two corresponding angular positions in the plane of rotation for a particular blade gave angular deflection in the tangential direction (i.e., the angle subtended by vector $\mathbf{d}_t$ in fig. 2). The tangential deflections were then spatially averaged over all blades. Depending on the model, the number of blades varied from 8 to 11.

Note that spatial averaging is necessary to eliminate a possible dynamic component resulting from the engine-order excitations. These signals cannot be eliminated by time averaging, which only removes the self-excited dynamic signals such as flutter. Even in the absence of any dynamic signals spatial and time averaging is desirable to reduce the random component of the signal.

Frequency Response Test

A special laboratory test was devised to determine whether the electronic circuit could respond fast enough at the conditions simulating the highest speed in the tests. The components in this experiment were identical to the ones in the propeller tests, except that a beam chopper was substituted for the propeller. The cable between the UDT amplifier and the tape recorder was of approximately the same length as in the tunnel tests. The laser beam was focused on the chopper blades near their outer periphery, and the direction of the beam was perpendicular to the plane of rotation. By placing the laser closer to this plane, a smaller beam diameter in this plane was achieved than in the propeller tests. Despite the fact that the chopper peripheral speed was lower than the peripheral speed in the test propellers, the net result was that the pulse rise and collapse times at the highest chopper speed were somewhat shorter than the minimum rise and collapse times in the propeller test.

An optical once-per-revolution signal was generated by drilling a small hole in the chopper disk area and focusing another laser beam on it. A photodiode detector was placed on the opposite side of the disk so that a positive pulse was generated every time the hole in the disk lined up with the beam. The signals were recorded on the FM, wideband II tape recorder and subsequently processed with the same software as in the tunnel tests.

Since the beam chopper blades do not deflect, in an ideal situation the average angular width of the blades should not vary with the chopper rotational speed. The reference rotational speed was 750 rpm, the maximum speed was 6000 rpm, and the average angular blade width for these two speeds was within $0.006°$ measured in the plane of rotation.

Analysis

Intersection of Laser Beam and Blade

It was shown that sufficient information is provided by initial conditions to obtain the equation of the laser beam in a relative frame of reference corresponding to either an instant when the beam is at a midchord (static test) or to an instant when the beam is tangent to the blade leading edge as shown in figure 2 (high-speed tests). The assumed form of the laser line equation was as follows:

$$Y = a_y X + b_y \tag{3}$$

$$Z = a_z X + b_z \tag{4}$$

That is, it was given as the intersection of a plane parallel to the Z axis and a plane parallel to the Y axis. From the coordinates of a leading- or trailing-edge finite-element line segment, an equation of a line containing this segment can be written in the following form:

$$X = c_x Y + d_x \tag{5}$$

$$Z = c_z Y + d_z \tag{6}$$

7

For convenience, the X, Y, and Z coordinates are expressed in terms of the polar cylindrical coordinates R, φ, and Y as follows:

$$R = \left(X^2 + Z^2\right)^{1/2}, \quad \varphi = \tan^{-1}\left(-\frac{X}{Z}\right) \tag{7}$$

where φ is positive opposite to the direction of rotation and the Y coordinate is the same. If the laser beam is rotated, a point on the line given by equations (3) and (4) will overlap with a point on the line given by equations (5) and (6), provided that Y and R are the same for these two points. Thus

$$[X^2(Y) + Z^2(Y)]_s = [X^2(Y) + Z^2(Y)]_\ell \tag{8}$$

where subscript s (blade segment) associates coordinates X and Z with equations (5) and (6) and subscript ℓ (laser beam) associates these coordinates with equations (3) and (4). Substituting these equations into equation (8) results in a quadratic equation given by

$$Y^2 + 2YP + Q = 0 \tag{9}$$

where

$$P = \frac{c_x d_x + c_z d_z - b_z \dfrac{a_z}{a_y} + b_y \dfrac{1 + a_z^2}{a_y^2}}{c_x^2 + c_z^2 - \dfrac{1 + a_z^2}{a_y^2}} \tag{10}$$

$$Q = \frac{d_x^2 + d_z^2 - b_z^2 + 2b_z b_y \dfrac{a_z}{a_y} - b_y^2 \dfrac{1 + a_z^2}{a_y^2}}{c_x^2 + c_z^2 - \dfrac{1 + a_z^2}{a_y^2}} \tag{11}$$

Once this equation is solved for Y, the blade segment point (subscript s) and the laser beam point (subscript ℓ) can be determined from equations (3) to (6).

All subsequent calculations were formulated by using the initial conditions of figure 2 (i.e., the beam is tangent to the leading edge). Because in the initial conditions for static tests the laser beam was directed to the midchord, it was necessary to rotate the beam in the direction of rotation until it was tangent to the leading edge. This changed coordinates X_ℓ and Z_ℓ, but X_s and Z_s remained the same at both the leading and trailing edges. They correspond to points A_{LE} and A_{TE} in figure 2. The new X_ℓ, Z_ℓ coordinates are identified with point A_{LE} and point E at the trailing edge. For this case, one also needs to compute angles β and γ in the new plane given by the triangle AAE.

In the actual computation X and Z for points A_{TE} and E are first transformed into polar coordinates R and φ. Then

$$\Delta\varphi_\delta = \Delta\varphi_{AE} = \varphi_A - \varphi_E \tag{12}$$

and the magnitude of vector δ is

$$|\delta| = 2R_A \sin\left(\frac{\Delta\varphi_\delta}{2}\right) \tag{13}$$

where the trailing edge in the subscript was omitted from R and the φ's. Equation (13) follows from the fact that vector δ is perpendicular to R at midpoint between points A_{TE} and E. (Note that in this report $\Delta\varphi_\delta$ is positive for either deflected or undeflected blade sections, as it is assumed that γ is positive and that $|\gamma| > |\theta|$.) Assuming that δ is oriented in the direction of rotation indicated in figure 2, the unit vector $\hat{\delta}$ is given by

$$\hat{\delta} = (\cos \varphi_{\delta/2}, 0, \sin \varphi_{\delta/2}) \tag{14}$$

where

$$\varphi_{\delta/2} = \varphi_A - \frac{\Delta\varphi_\delta}{2} \tag{15}$$

Chord vector $\mathbf{C}$ is computed by subtracting coordinates of points A at the leading and trailing edges; that is,

$$\mathbf{C} = (\mathbf{r}_A)_{LE} - (\mathbf{r}_A)_{TE} \tag{16}$$

Vector $\mathbf{V}_\ell$, which is coincident with the laser beam from point E to point A_{LE} in figure 2, can now be obtained from the following vector equation:

$$\mathbf{V}_\ell = \mathbf{C} - \delta \tag{17}$$

Because angles γ and β are always positive and less than 90°, they can be computed from the dot product of the respective adjoining unit vectors; that is,

$$\gamma = \cos^{-1}(\hat{\mathbf{C}} \cdot \hat{\mathbf{V}}_\ell) \tag{18}$$

$$\beta = \cos^{-1}(\hat{\delta} \cdot \hat{\mathbf{C}}) \tag{19}$$

Having obtained vector $\mathbf{V}_\ell$, one can now recompute the coefficients for equations (3) and (4) by projecting $\mathbf{V}_\ell$ onto the XY and XZ planes and using the fact that A_{LE} lies on the laser line. This completes the transformation of the initial conditions for the static test to the standard case as depicted in figure 2.

Once the predicted deflected-blade contour derived from the application of an aerostructural finite-element code is known, essentially the same method can be used to obtain the coordinates of points A′ in figure 2.

Angles $\Delta\varphi_{A'L}$ at the leading and trailing edges can be computed now for later reference. For the leading edge one must substitute Y, obtained from equation (9) as described previously for the deflected-blade geometry, into equation (3), which then together with equation (4) gives X_L and Z_L. Using equations (7) at points A′ and L at the leading edge then leads to

$$(\Delta\varphi_{A'L})_{LE} = (\Delta\varphi_t)_{LE} = (\varphi_{A'} - \varphi_L)_{LE} \tag{20}$$

The coordinates of point F at the trailing edge are obtained in a similar manner as those for point L at the leading edge. Then, using the polar coordinates of point A′ and F and noting that

$$(\Delta\varphi_{LF})_{TE} = (\Delta\varphi_{AE})_{TE} \tag{21}$$

yield

$$(\Delta\varphi_{A'L})_{TE} = (\Delta\varphi_t)_{TE} = (\varphi_{A'} - \varphi_F - \Delta\varphi_{AE})_{TE} \tag{22}$$

where $\Delta\varphi_{AE}$ is known from equation (12).

With

$$\Delta\varphi_{A'E'} = (\varphi_{A'})_{TE} - \varphi_F - (\Delta\varphi_{A'L})_{LE} = \Delta\varphi_{\delta'} \tag{23}$$

equations (13) to (15) can be used to obtain vector δ', the only qualification being that A and E in subscripts are now primed.

Having computed the leading- and trailing-edge coordinates of the undeflected and deflected blades and angles $\Delta\varphi_t$ allows one to construct the vector diagrams shown in figure 2.

Planar Geometry

In general, one cannot assume that all four leading- and trailing-edge points for the two blade sections in figure 2 lie in one plane. However, in order to illustrate the dependence of the measured deflections on the laser beam incidence angle γ and the blade angle β, this is assumed in this section. The resulting equations are also used as a first approximation in the iterative computation of blade twist and bending deflections from the experimental measurements. In the final computation, however, three-dimensional geometry is retained whenever possible and computations are performed in vector algebra.

As a part of initial conditions obtained from direct or indirect measurements, or through computation, one can assume that the angles β and γ are known and also that the coordinates of points A_{LE} and A_{TE} are known. The angles β and γ are assumed to be given in a plane defined by the laser beam unit vector $\hat{V}_\ell$ and the undeflected-blade chord unit vector $\hat{C}$. According to the present approximation, all deviations from this plane associated with the deflected-blade shape are assumed to be negligible. From these quantities and the measured values of $\Delta\varphi_t$ at the leading and trailing edges, one must compute estimates for bending deflections h and twist angle θ.

In figure 2 the deflected and undeflected chords are purposely shown to be different in length. Although this may be caused by the change in blade camber in the measurement plane, to a greater extent it is caused by the fact that the blade is free to slip relative to the laser beam as dictated by the geometry of the deflected blade and the beam. Because of the unequal sweeps at blade leading and trailing edges, any slip along the radial direction will be reflected in figure 2 as a change in the deflected-blade chord length. Even if the blades are swept equally at the leading and trailing edges, the apparent change in the chord length in the measurement plane can also be caused by an angular deformation such as the blade lean in the chordwise direction.

Experimental deflections and predicted finite-element deflections are compared in two phases. In the first phase predicted deflections are derived by using a blade section obtained by cutting the deflected-blade contour by a line coincident with the laser beam (in much the same way as it is done in the experiment by the laser beam). This makes it possible to evaluate the error associated with the apparent chord length change. (Note that this chord length change cannot be measured with only one laser per blade span.)

In the second phase deviations of predicted deflections obtained in this way, relative to true deflections obtained by strictly following the path of the original blade particles at the leading and trailing edges (corresponding to points A in fig. 2), are evaluated. The difference between these two deflections is referred to as the slip effect. However, its evaluation is reserved for a later section; this section deals only with the first-phase predicted results.

There are three displacement vector diagrams in figure 2. In the first, the total displacement d is resolved in the tangential direction and along the laser beam. Thus

$$\mathbf{d} = \mathbf{d}_t + \mathbf{d}_L \tag{24}$$

The second vector diagram, given by

$$\mathbf{d} = \mathbf{d}_c + \mathbf{h} \tag{25}$$

resolves vector $\mathbf{d}$ along the average chord direction and perpendicular to it. These two vector diagrams assume knowledge of deflected-blade coordinates A′, and therefore they can only be obtained for predicted results. In the experiment bending h and twist θ must be deduced from the measured tangential displacement d_t and the knowledge of angles β and γ. Estimates for h and θ are obtained by resolving $\mathbf{d}_t$ into components perpendicular to the average chord, $\mathbf{h}_t$, and along the laser beam, $\mathbf{d}_\ell$. Thus

$$\mathbf{d}_t = \mathbf{d}_\ell + \mathbf{h}_t \tag{26}$$

which is the third vector diagram in figure 2. Note that in the experiment quantities $\mathbf{h}$ or $\mathbf{d}$ cannot be obtained because $\mathbf{d}_L$ and $\mathbf{d}_c$ cannot be measured with one laser beam.

From figure 2 it follows that

$$h_t = \frac{d_t}{\sin \lambda} \sin \tau = \frac{d_t}{\sin \left(90 - \gamma - \dfrac{\theta}{2}\right)} \sin (\beta + \gamma)$$

$$= \frac{d_t}{\cos \left(\gamma + \dfrac{\theta}{2}\right)} \sin (\beta + \gamma) \tag{27}$$

Displacements h_t and d_t are signed magnitudes of vectors $\mathbf{h}_t$ and $\mathbf{d}_t$, where positive signs are selected when these displacements are as shown in figure 2. This is convenient because the general direction of the displacement can be obtained without referring to the associated vector or its unit vector. This convention is followed throughout the report. Note, however, that when constructing $\mathbf{h}_t$ by using unit vector $\hat{\mathbf{h}}_t$, for example, the absolute value of h_t must be taken; that is,

$$\mathbf{h}_t = |h_t| \hat{\mathbf{h}}_t \tag{28}$$

From equation (27) it follows that h_t and d_t will have the same sign for any reasonable values of β, γ, and θ.

Twist θ can be calculated from the following equation:

$$2C \sin \left(\frac{\theta}{2}\right) = (h_t)_{\text{TE}} - (h_t)_{\text{LE}} \tag{29}$$

Substituting equation (27) into equation (29) gives

$$2C \sin \left(\frac{\theta}{2}\right) = \left[(d_t)_{\text{TE}} - (d_t)_{\text{LE}} \right] \frac{\sin (\beta + \gamma)}{\cos \left(\gamma + \dfrac{\theta}{2}\right)} \tag{30}$$

When the d_t's are expressed in terms of R_A's and angles $\Delta \varphi_t$ (given by eqs. (20) and (22)), equation (30) becomes

$$2C \sin \left(\frac{\theta}{2}\right) = 2 \left[(R_A)_{\text{TE}} \sin \left(\frac{\Delta \varphi_t}{2}\right)_{\text{TE}} \right. \\ \left. - (R_A)_{\text{LE}} \sin \left(\frac{\Delta \varphi_t}{2}\right)_{\text{LE}} \right] \frac{\sin (\beta + \gamma)}{\cos \left(\gamma + \dfrac{\theta}{2}\right)} \tag{31}$$

A somewhat better approximation can be obtained if the subtraction indicated in the square brackets is performed in angular units. In this way contribution to θ because of unequal radii is avoided. The resulting equation is

$$C \sin \left(\frac{\theta}{2}\right) = (R_A)_{\text{TE}} \sin \left(\frac{\Delta^2 \varphi_t}{2}\right) \frac{\sin (\beta + \gamma)}{\cos \left(\gamma + \dfrac{\theta}{2}\right)} \tag{32}$$

where

$$\Delta^2 \varphi_t = (\Delta \varphi_t)_{\text{TE}} - (\Delta \varphi_t)_{\text{LE}} \tag{33}$$

In terms of experimental results $\Delta^2 \varphi_t$ can be interpreted (fig. 2) as the difference between trailing- and leading-edge angular deflections. It can also be interpreted as the difference in recorded pulse widths associated with the design and reference speeds, respectively; that is,

$$\Delta^2 \varphi_t = \Delta \varphi_{\delta'} - \Delta \varphi_\delta \tag{34}$$

It appears from equation (34) that $\Delta^2 \varphi_t$ and therefore twist θ can be obtained without knowing the $\Delta \varphi_t$'s. This in turn implies that twist can be determined without using the once-per-revolution signal. However, this signal is still needed for averaging and for transforming time units into angular units. When invoking the planar geometry approximation for twist in this report, it is implied that equation (32) is used to calculate it iteratively.

For predicted deflections, instead of equation (29) one has

$$2C_a \sin \left(\frac{\theta}{2}\right) = h_{\text{TE}} - h_{\text{LE}} \tag{35}$$

where

$$C_a = \frac{C' + C}{2} \tag{36}$$

is the average chord length. The difference between equations (29) and (35) can be found by expressing the h's in equation (35) in terms of h_t's. From figure 2 it follows that

$$(h_t - h)_{\text{TE}} = (d_c)_{\text{TE}} \tan \left(\gamma + \frac{\theta}{2}\right) \tag{37}$$

$$(h - h_t)_{\text{LE}} = (d_c)_{\text{LE}} \tan \left(\gamma + \frac{\theta}{2}\right) \tag{38}$$

and therefore

$$2C_a \sin\left(\frac{\theta}{2}\right) = (h_t)_{\text{TE}} - (h_t)_{\text{LE}}$$

$$- \left[(d_c)_{\text{TE}} + (d_c)_{\text{LE}}\right] \tan\left(\gamma + \frac{\theta}{2}\right) \quad (39)$$

Note that

$$(d_c)_{\text{TE}} + (d_c)_{\text{LE}} = C' - C \quad (40)$$

Substituting equations (36) and (40) into equation (39) results in

$$2C \sin\left(\frac{\theta}{2}\right) = (h_t)_{\text{TE}} - (h_t)_{\text{LE}} - (C' - C)$$

$$\times \left[\tan\left(\gamma + \frac{\theta}{2}\right) + \sin\left(\frac{\theta}{2}\right)\right] \quad (41)$$

The difference between equation (29) and equation (41) is in the last term. The correction angle for the twist can therefore be obtained with sufficient accuracy from

$$\theta_c = \frac{C' - C}{C} \left[\tan\left(\gamma + \frac{\theta}{2}\right) + \sin\left(\frac{\theta}{2}\right)\right] \quad (42)$$

where typically the first term in the square brackets is larger than the second because $\gamma > \theta/2$. Equations (37) and (38) can be considered as bending deflection corrections. These correction terms can be used to correct experimental deflections. They become increasingly more accurate the closer the experimental deflections are to the predicted deflections. The angle γ must be small enough to minimize the correction terms given by equations (37), (38), and (42) but be large enough to clearly separate the leading- and trailing-edge pulses throughout the measurement range.

Vector Diagrams

In this section, unlike in the preceding section, leading- and trailing-edge vector diagrams are allowed to be in different planes. However, equations (24) to (26) still hold.

Vector $\mathbf{d}$, the total predicted deflection at either the leading or trailing edge, is obtained by subtracting the point vectors at A' and A; that is,

$$\mathbf{d} = \mathbf{r}_{A'} - \mathbf{r}_A \quad (43)$$

The chord vector for the undeflected blade section is given by equation (16) and for the deflected section, by an analogous equation

$$\mathbf{C}' = (\mathbf{r}_{A'})_{\text{LE}} - (\mathbf{r}_{A'})_{\text{TE}} \quad (44)$$

The average chord is then

$$\mathbf{C}_a = \frac{\mathbf{C} + \mathbf{C}'}{2} \quad (45)$$

and the associated unit vector is

$$\hat{\mathbf{C}}_a = \frac{\mathbf{C}_a}{|\mathbf{C}_a|} \quad (46)$$

Vector $\mathbf{h}$ can now be obtained from the following equation:

$$\mathbf{h} = \mathbf{d} - \hat{\mathbf{C}}_a(\mathbf{d} \cdot \hat{\mathbf{C}}_a) \quad (47)$$

As in the preceding section bending displacement will be assigned a positive sign if it is as shown in figure 2. The sign of h is determined by the dot product of two unit vectors as follows:

$$S_h = \frac{\hat{\mathbf{n}}_{ch} \cdot \hat{\mathbf{n}}_{A_a}}{|\hat{\mathbf{n}}_{ch} \cdot \hat{\mathbf{n}}_{A_a}|} \quad (48)$$

where

$$\hat{\mathbf{n}}_{ch} = \hat{\mathbf{C}}_a \times \hat{\mathbf{h}} \quad (49)$$

$$\hat{\mathbf{n}}_{A_a} = \left(-\sin\frac{\varphi_A + \varphi_{A'}}{2}, \; 0, \; \cos\frac{\varphi_A + \varphi_{A'}}{2}\right) \quad (50)$$

and

$$h = S_h |\mathbf{h}| \quad (51)$$

at either the leading or the trailing edge. The determination of the sign of h, in the preceding equations, is based on the fact that in the limits of planar deformation $\hat{\mathbf{n}}_{ch}$ and $\hat{\mathbf{n}}_A$ are collinear.

Also presented in the report are bending deflections projected on a plane determined by the average tangential direction and the average chord direction. The average tangential direction is perpendicular to the average R direction given by

$$\varphi_a = \frac{(\varphi_A + \varphi_{A'})_{\text{LE}} + (\varphi_A + \varphi_{A'})_{\text{TE}}}{4} \quad (52)$$

The average tangential unit vector pointing in the direction of rotation is then defined by

$$\hat{\delta}_{ta} = (\cos \varphi_a, 0, \sin \varphi_a) \tag{53}$$

and the plane onto which bending deflections are projected is given by

$$\hat{n}_h = \frac{\hat{\delta}_{ta} \times \hat{C}_a}{|\hat{\delta}_{ta} \times \hat{C}_a|} \tag{54}$$

Then

$$h_p = h - \hat{n}_h(h \cdot \hat{n}_h) \tag{55}$$

gives the desired projection, where S_h (eq. (48)) can be taken to determine the sign of h_p.

Note that h was obtained from the total displacement, which is not known from the experimental measurements. It is therefore desirable to also compute the h_t component of the tangential displacement d_t so that it can be compared with the experimental h_t, which serves as the estimate of the bending deflection. Comparing the predicted h and h_t indicates how well h_t approximates h. To find the predicted h_t, one must first determine the vector d_t by using the $\Delta\varphi_t$ obtained as described in the section "Intersection of Laser Beam and Blade." The signed magnitude of d_t is given by

$$d_t = 2R_{A'} \sin\left(\frac{\Delta\varphi_t}{2}\right) \tag{56}$$

and the direction of d_t is determined by the unit vector

$$\hat{d}_t = (-S_t \cos \varphi_{t/2}, 0, -S_t \sin \varphi_{t/2}) \tag{57}$$

where

$$\varphi_{t/2} = \varphi_{A'} - \frac{\Delta\varphi_t}{2} \tag{58}$$

and

$$S_t = \frac{\Delta\varphi_t}{|\Delta\varphi_t|} \tag{59}$$

either at the leading or the trailing edge.

Vector h_t is obtained in the same way at the leading and trailing edges except that it is first necessary to rotate the laser beam unit vector at the trailing edge until it becomes tangent to the trailing edge, that is, by the angle subtended by δ as indicated in figure 2. The signed magnitude of h_t can be computed from the unit vector $\hat{h}_t$ defined by

$$\hat{n}_{t\ell} = \frac{\hat{d}_t \times \hat{V}_\ell}{|\hat{d}_t \times \hat{V}_\ell|} \tag{60}$$

$$\hat{h}_t = \frac{\hat{C}_a \times \hat{n}_{t\ell}}{|\hat{C}_a \times \hat{n}_{t\ell}|} \tag{61}$$

from the following equation:

$$h_t = \frac{d_t}{\hat{d}_t \cdot \hat{h}_t + \dfrac{|\hat{d}_t \cdot \hat{V}_\ell||\hat{h}_t \times \hat{d}_t|}{|\hat{d}_t \times \hat{V}_\ell|}} \tag{62}$$

The plane of h_t is defined by the unit normal vector $\hat{n}_t$ given by

$$\hat{n}_t = \frac{\hat{h}_t \times \hat{d}_t}{|\hat{h}_t \times \hat{d}_t|} \tag{63}$$

Projection of h_t onto the plane defined by the normal unit vector $\hat{n}_h$ is given by

$$h_{tp} = h_t - \hat{n}_h(h \cdot \hat{n}_h) \tag{64}$$

and the sign for h_{tp} can be taken to be the same as that for h_t. The component of d_t in the laser beam direction d_ℓ is computed from equation (26).

True Displacement of Leading and Trailing Edges

Up to this point predicted deflections were obtained by simulating the experiment (i.e., by cutting the finite-element, deflected-blade contour with a line coincident with the laser beam). However, even if predictions were obtained in this way, and even if they were exact and there were no measurement errors, one would still note a difference between these hypothetical predicted and measured deflections. This is largely due to the apparent change in blade chord length (already referred to in the section "Planar Geometry"), which cannot be measured with one laser beam. As shown later, one can use somewhat more general predicted results, obtained by including the three-dimensional effects, to estimate this error. However, the question still remains as to how predicted deflections obtained in this way compare with the rigorously derived deflections obtained by following the particular points at the leading and trailing edges, where the laser beam is tangent to the undeflected-blade contour.

The difference between these two deflections arises largely because the blade slips relative to the laser beam. It is desirable therefore to estimate this effect by using the calculated deflected-blade contour. As for the apparent chord length change estimate, this estimate becomes better the closer the experimental measurements are to the true deflections.

In terms of figure 2 points A and A′ are now associated with the same blade particle at both the leading and trailing edges. Given the coordinates of point A, the coordinates of point A′ are obtained by interpolating between the coordinates of the appropriate finite-element edge segments in undeflected and deflected positions.

The true displacement vector is differentiated from vector $\mathbf{d}$ by denoting it by $\bar{\mathbf{d}}$. Other quantities computed in this section are similarly differentiated from previously defined predicted quantities. With this change in nomenclature the equations presented in the section "Vector Diagrams" also apply here. Thus displacement vector $\bar{\mathbf{d}}$ can be obtained from equation (43), and the already outlined procedure (eqs. (44) to (51) and (25)) can be followed to resolve $\bar{\mathbf{d}}$ into components along the average chord direction and perpendicular to it. The second component represents the true bending displacement $\bar{\mathbf{h}}$. Unit vector $\hat{\mathbf{n}}_h$, which defines the average bending deflection plane, again is determined from equations (52) to (54). Thus the projection of the true $\bar{\mathbf{h}}$ onto this plane ($\bar{\mathbf{h}}_p$), from equation (55), can be computed.

Computation of Twist Angle

As for leading- and trailing-edge displacements, predicted twist is obtained first by using the undeflected- and deflected-blade contours as described by a finite-element model. A similar procedure is used for the measured data, but because of coupling between twist and bending it involves iterative calculations. This order of presentation also allows the errors inherent in the experimental procedure to be illustrated before the data are analyzed.

Predicted twist is evaluated as an angular displacement of the deflected-blade chord vector $\mathbf{C}′$ relative to the undeflected-blade chord vector $\mathbf{C}$. Because experimental twist is associated with a plane that may or may not coincide with the plane of the total predicted twist, predicted twist is projected onto several planes. The appropriate plane for comparing experimental and predicted deflections is selected so that the error caused by the slip effect is minimized.

In figure 2 the two laser beams tangent to points A and A′ at the leading edge are rotated about the Y axis by the angle $\Delta\varphi_t$ with respect to each other. If the undeflected-blade chord vector is rotated by the same amount before the twist is computed, the resulting twist is called relative. Otherwise, the computed twist is referred to as the absolute twist. Relative twist is included because it follows more readily from the experimental data, and it is therefore of some interest to determine the difference between it and the absolute twist.

Absolute and relative twists are calculated in the same way whether the laser beam slip is included in the predicted deflections or excluded (i.e., the true twist). One only has to use the appropriate coordinates A′, the correct deflected-blade chord length $C′$, and the associated vector diagrams. The equation for absolute twist is

$$\left|\theta_{n_c}\right| = \tan^{-1}\left(\frac{|\mathbf{C}′ \times \mathbf{C}|}{|\mathbf{C}′ \cdot \mathbf{C}|}\right) \tag{65}$$

The plane and the sign of twist are determined by a unit vector given by

$$\hat{\mathbf{n}}_c = \frac{\mathbf{C}′ \times \mathbf{C}}{|\mathbf{C}′ \times \mathbf{C}|} \tag{66}$$

Twist θ_{n_c} is also projected onto a plane perpendicular to the unit vector defined by

$$\hat{\mathbf{n}}_{c\ell} = \frac{\mathbf{C} \times \hat{\mathbf{V}}_\ell}{|\mathbf{C} \times \hat{\mathbf{V}}_\ell|} \tag{67}$$

and onto planes perpendicular to unit vectors $\hat{\mathbf{n}}_h$ and $\hat{\mathbf{k}}$. The last plane is therefore the XY plane, perpendicular to the pitch axis. The desired projections of the appropriate chord vectors are given by

$$\mathbf{C}_n = \mathbf{C} - \hat{\mathbf{n}}(\mathbf{C} \cdot \hat{\mathbf{n}}) \tag{68}$$

$$\mathbf{C}_n′ = \mathbf{C}′ - \hat{\mathbf{n}}(\mathbf{C}′ \cdot \hat{\mathbf{n}}) \tag{69}$$

where either $n_{c\ell}$, n_h, or k should be substituted for n. The associated signed twist angles are given by

$$\theta_n = \tan^{-1}\left[\frac{(\mathbf{C}_n′ \times \mathbf{C}_n) \cdot \hat{\mathbf{n}}}{\mathbf{C}_n′ \cdot \mathbf{C}_n}\right] \tag{70}$$

where, again, indicated substitution for n should be performed.

Note that instead of using the projected plane vectors to compute θ_n, one could also project vector θ_{n_c} given by equations (65) and (66) onto the desired plane. However, the difference is very slight (of the order of a hundredth of a degree) and is of no practical significance.

As already mentioned, projected twists will be useful in optimizing the experimental analysis procedure. Note that the projected vectors given by equations (68) and (69) are not unit vectors. If desired, they can be appropriately normalized before the twist deflections are computed.

For relative twist to be obtained, unit vectors $\hat{\mathbf{V}}_\ell$ and $\hat{\mathbf{C}}$ must be first rotated by the angle $(\Delta\varphi_\ell)_{LE}$ in the XZ plane, as indicated in figure 2. With this restriction equations (65) to (70) apply.

Experimental Deflections

It is desirable to use the same set of equations for computing the predicted and experimental twist angles. Before the

equations in the previous section can be applied, the deflected-blade chord vector C' must be known. However, in the experiment the coordinates of points A' and the deflected-blade chord vector are unknown and must be obtained from some preliminary estimates of deflections before beginning the iteration procedure. As an initial estimate of the twist angle, equations (32) and (33) are used as described in the section "Planar Geometry." The angles $\Delta\tilde{\varphi}_t$ for the leading and trailing edges needed in equation (33) are known from the experiment. (A tilde is used over experimentally derived quantities to clearly differentiate them from predicted quantities.) They are obtained, as described in the section "Experimental Data Reduction," by using spatial and time averaging.

Initial variables associated with the undeflected blade and the laser beam geometry are the same as for predicted results. In particular, one can assume that vector $\tilde{n}_{c\ell}$ is known from equation (67). By defining another unit vector in this plane, tangent to $\hat{C}$, one can rotate $\hat{C}$ by $\tilde{\theta}/2$, as shown in figure 8, to obtain the vector $C_{\theta/2}$ or, after normalization, the associated unit vector $\tilde{\hat{C}}_a$. The initial estimate for $\tilde{\theta}$ was obtained as described in the section "Planar Geometry." The equations for this rotation are

$$\hat{t}_{cn} = \frac{\hat{C} \times \hat{n}_{c\ell}}{|\hat{C} \times \hat{n}_{c\ell}|} \tag{71}$$

$$C_{\theta/2} = \hat{C} + \frac{\hat{t}_{cn} \sin \tilde{\theta} - 2\hat{C} \sin^2\left(\dfrac{\tilde{\theta}}{2}\right)}{2} \tag{72}$$

$$\tilde{\hat{C}}_a = \frac{C_{\theta/2}}{|C_{\theta/2}|} \tag{73}$$

The signed magnitude of vector $\tilde{d}_t$ is obtained from the following equation:

$$\tilde{d}_t = 2R_A \sin \frac{\Delta\tilde{\varphi}_t}{2} \tag{74}$$

The unit vector describing the direction of vector $\tilde{d}_t$ is given by

$$\tilde{\hat{d}}_t = (-\tilde{S}_t \cos \tilde{\varphi}_{t/2}, 0, -\tilde{S}_t \sin \varphi_{t/2}) \tag{75}$$

where

$$\tilde{\varphi}_{t/2} = \varphi_A + \frac{\Delta\tilde{\varphi}_t}{2} \tag{76}$$

and

$$\tilde{S}_t = \frac{\Delta\tilde{\varphi}_t}{|\Delta\tilde{\varphi}_t|} \tag{77}$$
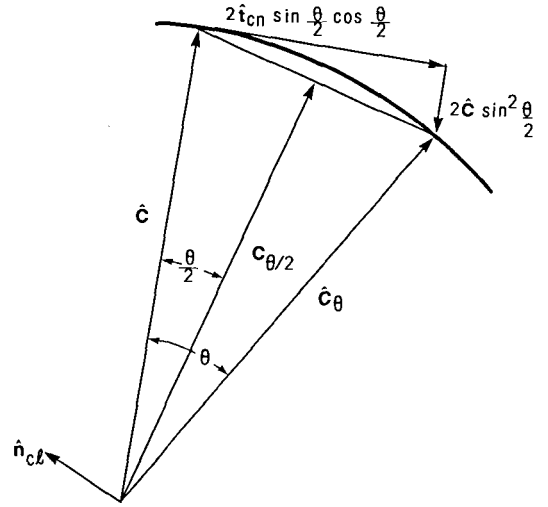
Figure 8.—Rotation of unit vector $\hat{C}$.

The subscripts for the leading and trailing edges were left out since both apply. Sufficient information is now available so that equations (60) to (64) and (26) can be applied to obtaining the $\tilde{h}_t$ and $\tilde{d}_\ell$ components of $\tilde{d}_t$. As in the section "Vector Diagrams," before the equations can be applied at the trailing edge, the unit vector in the laser direction must be rotated by the angle $\Delta\tilde{\varphi}_\delta$, as indicated in figure 2.

The coordinates of points A' are estimated by using $\tilde{h}_t$ instead of the unknown d. Thus

$$\tilde{r}_{A'} = r_A + \tilde{h}_t \tag{78}$$

at either the leading or the trailing edge. One can now obtain the deflected chord vector from the following equation:

$$\tilde{C}' = (\tilde{r}_{A'})_{LE} - (\tilde{r}_{A'})_{TE} \tag{79}$$

and recalculate the magnitude of $\tilde{d}_t$ and angle $\tilde{\varphi}_{t/2}$ as follows:

$$\tilde{d}_t = 2R_{A'} \sin\left(\frac{\Delta\tilde{\varphi}_t}{2}\right) \tag{80}$$

$$\tilde{\varphi}_{t/2} = \tilde{\varphi}_{A'} - \frac{\Delta\tilde{\varphi}_t}{2} \tag{81}$$

Equations (75), (45), (60) to (64), (26), (78), and (81) can now be applied again to obtain a better estimate for the deflected-blade chord vector. Actually, two iterations were carried out, with the second iteration giving virtually the same results as the first.

Once the deflected-blade chord vector is obtained, the computation of relative and absolute twists follows the procedure outlined in the section "Computation of Twist Angle." Vector $\tilde{h}_t$ is also projected on the average deflection plane $\tilde{n}_h$ as described by equations (52) to (54) and (64).

Results

Experimental Variables

For the static test of the SR–7L propeller, results were obtained at the three blade radii: near the tip, near the 3/4 radius, and near the 1/2 radius. The exact positions, determined by the leading- and trailing-edge Z coordinates normalized with the maximum value of Z at the leading edge, are given in table I(a). As indicated in the table ("span position" column), these stations are numbered consecutively, starting with the number 1 at the tip. Also given in the table are the nominal blade setting angles β_{nom} and the rotational speeds (design value and the values normalized with respect to design). These quantities determine the initial conditions and are given for both predicted and experimental results. At each blade angle setting rotational speed was varied in several steps from a low reference value to the maximum value indicated in the table. Note that for the two higher blade angles predicted results were actually obtained for β_{nom} of 33.3° and 25.5° as shown in table I(a). However, these values were judged to be sufficiently close to the test values of 32° and 25.8°, particularly considering differences between predicted and measured deflections.

The complete results of the high-speed test are given for three blades designated as F11, F1, and F7, which are all forward rotors of the twin-rotor counterrotating propeller model. All results presented are for the near-tip station. As in the static test the propeller speed was varied from a low reference speed to the design value. However, for the F11

blade the rotor speed achieved in the test was only 0.952 of the design. (The corresponding aft rotor speed was 0.965 of the design.) Table I(b) lists the initial conditions for this test. The Z coordinate was also normalized by using its maximum value at the leading edge.

Detailed results for the displacements of the leading and trailing edges normal to the average chord direction and the absolute and relative twist angles are presented first in tabular form for the design (or maximum) speeds. Deflections are then presented graphically to illustrate their variation with speed and the agreement between experimental and predicted values.

In addition to experimental deflections the tables include calculated deflections that incorporate the laser beam slip effect (discussed in the section "Planar Geometry") and the rigorous deflections obtained by strictly following leading- and trailing-edge blade particles (discussed in the section "True Displacement of Leading and Trailing Edges"). By comparing these two deflections one can evaluate the error associated with the laser beam slip. The tables for twist angles also include predicted results calculated for the constant-chord-length assumption. Hence the effect of this assumption can also be evaluated. (This assumption is used when calculating twist from experimental data.)

Leading- and Trailing-Edge Displacements

Leading- and trailing-edge displacements perpendicular to the chord (i.e., bending displacements) are given for the static test of the SR–7L propeller in table II for blade angles of 22°, 32°, and 25.8° and for the high-speed test in table III. The

TABLE I.—TEST VARIABLES

(a) Static test, SR–7L blade.

Design rotational speed, rpm	Speed fraction		Nominal blade angle, β_{nom}		Span position	Z/Z_{max} fraction	
	Test	Prediction	Test	Prediction		Leading edge	Trailing edge
1698	1.005	1.000	22.0	22.0	1	0.969	0.956
					2	.758	.752
					3	.571	.562
1698	1.013	1.000	32.0	33.3	1	0.968	0.960
					3	.561	.555
2038	1.202	1.200	25.8	25.5	1	0.968	0.959
					2	.759	.754
					3	.576	.567

(b) High-speed tests.

Blade	Design rotational speed, rpm	Speed fraction		Nominal blade angle, β_{nom}	Mach number	Z/Z_{max} fraction	
		Test	Prediction			Leading edge	Trailing edge
F11	8089	0.952	1.000	60.3	0.80	0.973	0.960
F1	8185	.996	1.000	57.1	.72	.975	.973
F7	8314	.993	1.000	58.5	.72	.963	.961

TABLE II.—BENDING DEFLECTIONS—SR-7L BLADE, STATIC TEST

[In each group of numbers, the top row is for the leading edge and the bottom row for the trailing edge.]

(a) Blade angle $\beta = 22°$

Span position	Symbol	Plane	True predicted $\bar{h}$, cm	True predicted $\hat{\bar{n}}$ $\hat{i}$	$\hat{j}$	$\hat{k}$	Predicted with slip h, cm	Predicted with slip $\hat{n}$ $\hat{i}$	$\hat{j}$	$\hat{k}$	Experimental (relative to reference point) $\bar{h}$, cm	Experimental $\hat{\bar{n}}$ $\hat{i}$	$\hat{j}$	$\hat{k}$
1	h	$\hat{n}_{ch}$	−0.7943	−0.1664	0.2893	0.9427	−0.7765	−0.1457	0.2149	0.9657	------	------	------	-----
			−.5911	−.2576	.6082	.7508	−.5088	−.2080	.4228	.8820	------	------	------	-----
	h_p	$\hat{n}_h$	−.7938	−.1771	.3248	.9290	−.7714	−.1774	.3188	.9311	------	------	------	-----
			−.5560	−.1771	.3248	.9290	−.5052	−.1774	.3188	.9311	------	------	------	-----
	h_t	$\hat{n}_t$	------	------	------	-----	−.8880	−.1153	.2514	.9610	−0.4364	−0.1165	0.2533	0.9603
			------	------	------	-----	−.5928	−.2406	.3755	.8950	.1130	−.2405	.3752	.8952
	h_{tp}	$\hat{n}_h$	------	------	------	-----	−.8844	−.1774	.3188	.9311	−.4348	−.1797	.3161	.9315
			------	------	------	-----	−.5908	−.1774	.3188	.9311	.1125	−.1797	.3161	.9315
2	h	$\hat{n}_{ch}$	−1.3752	−0.0234	0.0225	0.9995	−1.3909	0.0725	−0.1920	0.9787	------	------	------	-----
			−1.4130	−.1057	.2200	.9698	−1.4529	−.1610	.3675	.9160	------	------	------	-----
	h_p	$\hat{n}_h$	−1.3708	−.0537	.0950	.9940	−1.3175	−.0530	.1076	.9928	------	------	------	-----
			−1.3995	−.0537	.0950	.9940	−1.3909	−.0530	.1076	.9928	------	------	------	-----
	h_t	$\hat{n}_t$	------	------	------	-----	−1.4516	.1618	−.1282	.9793	−1.2123	0.1599	−0.1187	0.9800
			------	------	------	-----	−1.4653	−.2690	.3118	.9113	−.7343	−.2673	.3090	.9127
	h_{tp}	$\hat{n}_h$	------	------	------	-----	−1.3881	−.0530	.1076	.9928	−1.1615	−.0550	.1044	.9930
			------	------	------	-----	−1.4061	−.0530	.1076	.9928	−.7051	−.0550	.1044	.9930
3	h	$\hat{n}_{ch}$	−0.6393	−0.0533	0.0508	0.9973	−0.9091	0.3765	−0.6857	0.6229	------	------	------	-----
			−.2835	−.1313	.1906	.9728	−.3703	−.3830	.6639	.6423	------	------	------	-----
	h_p	$\hat{n}_h$	−.6279	.0399	−.1147	.9926	−.6386	.0409	−.0989	.9943	------	------	------	-----
			−.2659	.0399	−.1147	.9926	−.2065	.0409	−.0989	.9943	------	------	------	-----
	h_t	$\hat{n}_t$	------	------	------	-----	−.9101	.2133	−.7711	.6000	−0.8489	0.2132	−0.7708	0.6003
			------	------	------	-----	−.3683	−.1852	.7185	.6704	.1052	−.1835	.7155	.6741
	h_{tp}	$\hat{n}_h$	------	------	------	-----	−.6309	.0409	.0989	.9943	−.5921	.0401	−.1053	.9936
			------	------	------	-----	−.2210	.0409	.0989	.9943	.0630	.0401	−.1053	.9936

(b) Blade angle $\beta = 32°$

Span position	Symbol	Plane	True predicted $\bar{h}$, cm	True predicted $\hat{\bar{n}}$ $\hat{i}$	$\hat{j}$	$\hat{k}$	Predicted with slip h, cm	Predicted with slip $\hat{n}$ $\hat{i}$	$\hat{j}$	$\hat{k}$	Experimental (relative to reference point) $\bar{h}$, cm	Experimental $\hat{\bar{n}}$ $\hat{i}$	$\hat{j}$	$\hat{k}$
1	h	$\hat{n}_{ch}$	1.0170	0.0326	−0.1662	0.9855	1.0036	−0.1515	0.1462	0.9776	------	------	------	-----
			1.5326	.0082	−.1236	.9923	1.5608	−.2098	.2537	.9442	------	------	------	-----
	h_p	$\hat{n}_h$	.9228	−.1770	.2085	.9619	1.0020	−.1770	.1928	.9651	------	------	------	-----
			1.4211	−.1770	.2085	.9619	1.5568	−.1770	.1928	.9651	------	------	------	-----
	h_t	$\hat{n}_t$	------	------	------	-----	.8804	−.1070	.1467	.9834	−0.1593	−0.1119	0.1535	0.9818
			------	------	------	-----	1.5514	−.2345	.2407	.9418	.5164	−.2362	.2415	.9412
	h_{tp}	$\hat{n}_h$	------	------	------	-----	.8778	−.1770	.1928	.9651	−.1590	−.1757	.1976	.9644
			------	------	------	-----	1.5474	−.1770	.1928	.9651	.5151	−.1757	.1976	.9644
3	h	$\hat{n}_{ch}$	−0.4196	−0.1342	0.1326	0.9820	−0.4826	0.3935	−0.4693	0.7905	------	------	------	-----
			.0818	.2461	−.3057	.9198	.0688	−.2358	.2550	.9377	------	------	------	-----
	h_p	$\hat{n}_h$	−.4056	.0346	−.0629	.9974	−.4006	.0350	−.0591	.9976	------	------	------	-----
			.0775	.0346	−.0629	.9974	.0630	.0350	−.0591	.9976	------	------	------	-----
	h_t	$\hat{n}_t$	------	------	------	-----	−.4846	.2453	−.5729	.7821	−0.6190	0.2438	−0.5801	0.7772
			------	------	------	-----	.0617	−.2016	.5098	.8364	.2210	−.1996	.5172	.8322
	h_{tp}	$\hat{n}_h$	------	------	------	-----	−.4054	.0350	−.0591	.9976	−.5154	.0352	−.0597	.9976
			------	------	------	-----	.0503	.0350	−.0591	.9976	.1786	.0352	−.0597	.9976

TABLE II.—Concluded.

(c) Blade angle $\beta = 25.8°$

Span position	Symbol	Plane	True predicted $\bar{h}$, cm	True predicted $\hat{\bar{n}}$ $\hat{i}$	$\hat{j}$	$\hat{k}$	Predicted with slip h, cm	Predicted with slip $\hat{n}$ $\hat{i}$	$\hat{j}$	$\hat{k}$	Experimental (relative to reference point) $\tilde{h}$, cm	Experimental $\hat{\bar{n}}$ $\hat{i}$	$\hat{j}$	$\hat{k}$
1	h	$\hat{n}_{ch}$	−0.3078	−0.3704	0.8766	0.3073	−0.1125	−0.0525	−0.0394	0.9978	------	------	------	-----
			.4780	.2784	−.7834	.5556	.2507	−.1889	.3125	.9309	------	------	------	----
	h_p	$\hat{n}_h$	−.1885	−.1773	.2942	.9391	−.1057	−.1774	.2818	.9429	------	------	------	----
			.1156	−.1773	.2942	.9391	.2507	−.1774	.2818	.9429	------	------	------	----
	h_t	$\hat{n}_t$	------	------	------	-----	−.2550	−.1102	.2131	.9708	0.0277	−0.1136	0.2186	0.9692
			------	------	------	-----	.1880	−.2379	.3418	.9091	.8169	−.2378	.3418	.9092
	h_{tp}	$\hat{n}_h$	------	------	------	-----	−.2537	−.1774	.2818	.9429	.0277	−.1797	.2810	.9427
			------	------	------	-----	.1872	−.1774	.2818	.9429	.8138	−.1797	.2810	.9427
2	h	$\hat{n}_{ch}$	−1.4460	−0.0339	0.0433	0.9985	−1.4600	0.0810	−0.1798	0.9804	------	------	------	-----
			−1.3272	−.1324	.2454	.9603	−1.3526	−.1741	.3422	.9234	------	------	------	-----
	h_p	$\hat{n}_h$	−1.4442	−.0554	.0872	.9946	−1.3904	−.0546	.0972	.9938	------	------	------	-----
			−1.3058	−.0554	.0872	.9946	−1.2990	−.0546	.0972	.9938	------	------	------	-----
	h_t	$\hat{n}_t$	------	------	------	-----	−1.5141	.1545	−.1176	.9810	−1.4346	0.1520	−0.1140	0.9818
			------	------	------	-----	−1.3619	−.2651	.2897	.9197	−.5316	−.2635	.2873	.9209
	h_{tp}	$\hat{n}_h$	------	------	------	-----	−1.4524	−.0546	.0972	.9938	−1.3785	−.0566	.0948	.9939
			------	------	------	-----	−1.3101	−.0546	.0972	.9938	−.5118	−.0566	.0948	.9939
3	h	$\hat{n}_{ch}$	−0.7808	−0.0790	0.0827	.9934	−1.0660	0.3979	−0.6384	0.6592	------	------	------	-----
			−.2047	−.2254	.3148	.9220	−.2670	−.4284	.6546	.6229	------	------	------	-----
	h_p	$\hat{n}_h$	−.7633	.0354	−.0964	.9947	−.7709	.0367	−.0815	.9960	------	------	------	-----
			−.1801	.0354	−.0964	.9947	−.1471	.0367	−.0815	.9960	------	------	------	-----
	h_t	$\hat{n}_t$	------	------	------	-----	−1.0663	.2103	−.7524	.6242	−1.1422	0.2099	−0.7516	0.6253
			------	------	------	-----	−.2649	−.1829	.7055	.6847	.3287	−.1809	.7023	.6885
	h_{tp}	$\hat{n}_h$	------	------	------	-----	−.7551	.0367	−.0815	.9960	−.8136	.0358	−.0870	.9956
			------	------	------	-----	−.1684	.0367	−.0815	.9960	.2088	.0358	−.0870	.9956

TABLE III.—BENDING DEFLECTIONS—HIGH-SPEED TEST

| Blade	Symbol	Plane	True predicted $\bar{h}$, cm	$\hat{\bar{n}}$ $\hat{i}$	$\hat{j}$	$\hat{k}$	Predicted with slip h, cm	$\hat{n}$ $\hat{i}$	$\hat{j}$	$\hat{k}$	Experimental (relative to reference point) $\tilde{h}$, cm	$\hat{\tilde{n}}$ $\hat{i}$	$\hat{j}$	$\hat{k}$
F11	h	$\hat{n}_{ch}$	0.6375	−0.0601	−0.0801	0.9950	0.6347	−0.0970	−0.0550	0.9938	-----	------	------	-----
			.8334	−.1051	−.0423	.9936	.8245	−.1704	.0073	.9853	-----	------	------	-----
	h_p	$\hat{n}_h$	.6345	−.1342	−.0176	.9908	.6340	−.1338	−.0239	.9907	-----	------	------	-----
			.8329	−.1342	−.0176	.9908	.8235	−.1338	−.0239	.9907	-----	------	------	-----
	h_t	$\hat{n}_t$	-----	------	------	-----	.6543	−.0844	−.0345	.9958	0.7419	−0.0837	−0.0349	0.9959
			-----	------	------	-----	.8486	−.1762	−.0019	.9843	.8903	−.1748	−.0026	.9846
	h_{tp}	$\hat{n}_h$	-----	------	------	-----	.6535	−.1338	−.0239	.9907	.7412	−.1339	−.0244	.9907
			-----	------	------	-----	.8479	−.1338	−.0239	.9907	.8893	−.1339	−.0244	.9907
F1	h	$\hat{n}_{ch}$	0.5311	−0.0448	0.0133	0.9989	0.5314	−0.0545	0.0183	0.9983	-----	------	------	-----
			.7506	−.0920	.0621	.9938	.7470	−.1291	.0953	.9870	-----	------	------	-----
	h_p	$\hat{n}_h$	.5298	−.0927	.0627	.9937	.5306	−.0926	.0575	.9940	-----	------	------	-----
			.7506	−.0927	.0627	.9937	.7460	−.0926	.0575	.9940	-----	------	------	-----
	h_t	$\hat{n}_t$	-----	------	------	-----	.5710	−.0376	.0457	.9982	0.7196	−0.0359	0.0448	0.9983
			-----	------	------	-----	.7851	−.1405	.0796	.9869	1.0414	−.1393	.0789	.9871
	h_{tp}	$\hat{n}_h$	-----	------	------	-----	.5702	−.0926	.0575	.9940	.7186	−.0936	.0560	.9940
			-----	------	------	-----	.7841	−.0926	.0575	.9940	1.0404	−.0936	.0560	.9940
F7	h	$\hat{n}_{ch}$	0.8816	−0.0255	−0.0058	0.9997	0.8806	−0.0522	0.0100	0.9986	-----	------	------	-----
			.9698	−.0629	.0268	.9977	.9642	−.1238	.0723	.9897	-----	------	------	-----
	h_p	$\hat{n}_h$	.8786	−.0879	.0485	.9950	.8796	−.0877	.0408	.9953	-----	------	------	-----
			.9693	−.0879	.0485	.9950	.9629	−.0877	.0408	.9953	-----	------	------	-----
	h_t	$\hat{n}_t$	-----	------	------	-----	.9144	−.0382	.0329	.9987	1.1984	−0.0372	0.0324	0.9988
			-----	------	------	-----	1.0124	−.1286	.0635	.9896	1.4879	−.1279	.0631	.9898
	h_{tp}	$\hat{n}_h$	-----	------	------	-----	.9134	−.0877	.0408	.9953	1.1971	−.0906	.0386	.9951
			-----	------	------	-----	1.0114	−.0877	.0408	.9953	1.4864	−.0906	.0386	.9951

table includes signed deflections and the associated normal unit vectors that define the appropriate planes. Modified h and $\hat{n}$ symbols in the column headings allow the differentiation between three types of tabulated results. As mentioned previously, a bar above a symbol indicates the no-slip condition, a tilde indicates experimental results, and unmodified h and $\hat{n}$ indicate predicted results with the slip effect.

The reference speed for the high-speed test proved to be sufficiently low so that deflections at that speed could be neglected. However, the reference speed for the static test was about 40 percent of the design, and the deflections at that speed were not negligible, although they were relatively small. (The limitation on low-speed operation was inherent in the test rig.) This was compensated for by first obtaining the deflections at reference speed through graphical extrapolation. The experimental results in figures 9 and 10 were then replotted to include these deflections. The lowest speed point in each figure corresponds to the reference speed, and its ordinate indicates by how much each experimental point was shifted to adjust for reference speed deflection. Thus the deflections

plotted in these figures are absolute. However, in the table the signed measured deflections are as originally calculated, assuming no deflection at the reference speed. Hence these deflections are relative to the reference point. Deflections in figures 9 and 10 are given as a function of the square of the ratio of the rotational speed to the design rotational speed N_f^2. Also included from table II are the true predicted deflections projected on plane $\hat{\bar{n}}_h$.

In table III the test speed for the F11 rotor was, as already mentioned, 95.2 percent of the design; however, only predicted results at the design speed were available. To evaluate the quantitative agreement between predicted and experimental results, one should extrapolate the deflections to the design speed in figure 10. Predicted results for this rotor were included in the table mainly to evaluate the slip effect error.

Deflections h_t in tables II and III were not calculated for the no-slip condition because the definition of h_t requires some slip along the blade relative to the original undeflected reference point. On the other hand, $\tilde{h}$ was not available for the experimental results because the measurement is performed
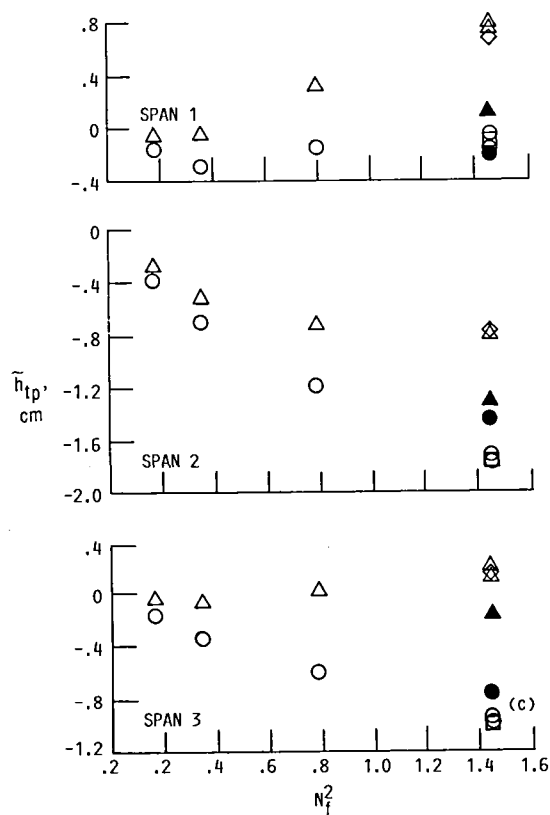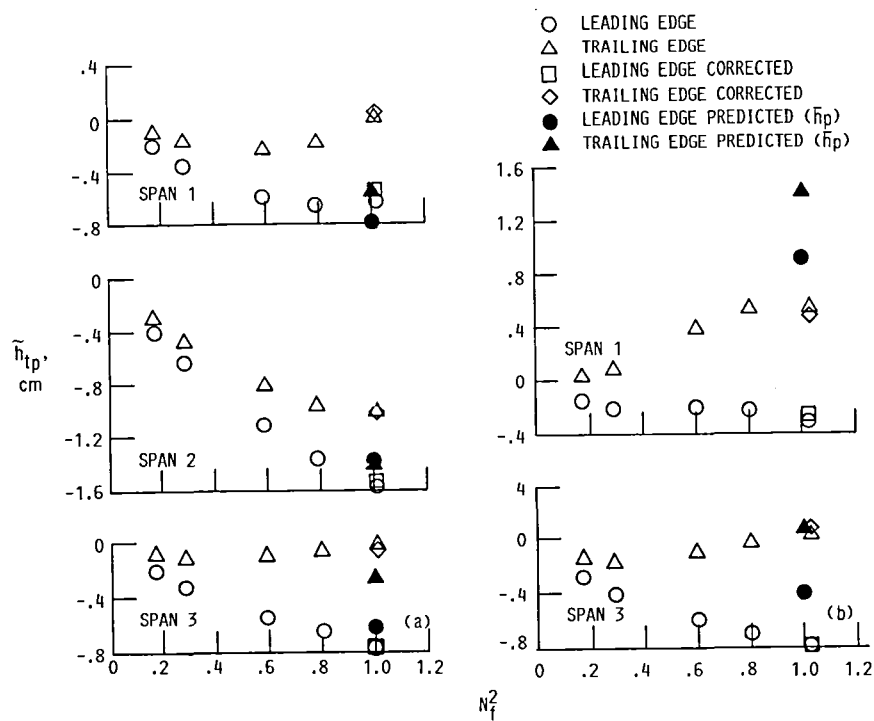
(a) Blade angle $\beta = 22°$.
(b) Blade angle $\beta = 32°$.
(c) Blade angle $\beta = 25.8°$.

Figure 9.—Bending deflections—SR-7L blade, static test.

LEADING EDGE ○
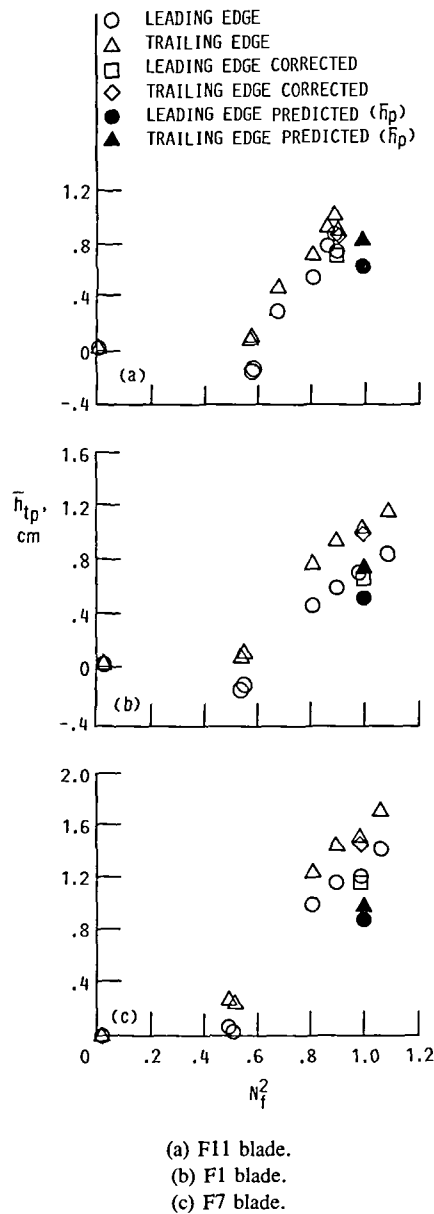TRAILING EDGE △
LEADING EDGE CORRECTED □
TRAILING EDGE CORRECTED ◇
LEADING EDGE PREDICTED $(\bar{h}_p)$ ●
TRAILING EDGE PREDICTED $(\bar{h}_p)$ ▲

(a) F11 blade.
(b) F1 blade.
(c) F7 blade.

Figure 10.—Bending deflections—high-speed test.

with only one laser beam and $\tilde{h}_t$ must serve as an approximation to $\tilde{h}$.

Note that the deflections in table II are approximately of the same order of magnitude as those in table III. However, since the deflections have not been nondimensionalized and the rotor diameters in the high-speed test were about 4.5 times smaller, it is obvious that the deflections in table III are relatively more significant than those in table II.

The slip effect can be evaluated by first examining the two predicted results associated with h and $\tilde{h}$. For the stiff SR-7L blade in the static test (table II) there appears to be a significant difference between h and $\tilde{h}$ at span position 3 for $\beta = 22°$ and at span positions 1 and 3 for $\beta = 25.8°$. For the $\hat{n}_{ch}$'s the largest difference is at the tip (span position 1), particularly for $\beta = 25.8°$. On the other hand, for the less stiff F11, F1,

and F7 blades in table III there is no significant difference in h's or the corresponding unit vectors. The results in table II therefore must be confined to a plane. Thus, choosing average bending planes as defined by $\bar{n}_h$ and $\hat{n}_h$ and projecting the associated displacement vectors onto these planes, one finds that the difference between the two predicted results becomes small both in magnitude ($\bar{h}_p$ and h_p) and in the unit plane-vector direction ($\bar{n}_h$ and $\hat{n}_h$).

Examining predicted results with slip, in the central portion of tables II and III, shows that the difference between h_p and h_{tp} is fairly small for all blades at both the leading and trailing edges. Results discussed in the previous paragraph then imply that the difference between $\bar{h}_p$ and h_{tp} is also small. Therefore, one can expect small systematic error when estimating $\bar{h}_p$ with $\bar{h}_{tp}$. This provides a justification for the inclusion of $\bar{h}_{tp}$ and $\bar{h}_p$ in figures 9 and 10. (Note again that in the figures deflections are absolute.) Included in the figures are corrected deflections at maximum speed (square and diamond symbols).

Twist Angles

Tables IV to VII present results for absolute and relative twist angles. (Note that positive twist corresponds to a blade angle β increase relative to the reference value.) Although most of the discussion refers to the absolute twist, it also applies to the relative twist angles. As shown later, the difference between relative and absolute angles for the optimum measurement plane is small.

As noted in the first group of columns in these tables, in addition to the apparent total twist angle (plane $\hat{n}_c$), twist angles in the initial plane $\hat{n}_{c\ell}$, the average bending plane $\hat{n}_h$, and perpendicular to the pitch axis $\hat{k}$ are also given. The first three groups of columns from the left are associated with the same results as for bending (i.e., with the true predicted twist angle, the predicted twist angle that includes the laser beam slip effect, and the measured absolute twist). The fourth group of columns was added in these tables to evaluate the effect of the constant-chord-length assumption made in calculating twist angles from measurements. The explicit expression for the associated correction factor was derived (eq. (42)) for the planar geometry case. Here θ_n'' and $\hat{n}''$ are derived identically as in the experiment except that the measured angles in the tangential direction $\Delta\varphi_t$ are obtained from predicted blade contours. Thus subtracting θ_n from θ_n'' gives the correction factor analogous to the one for the planar geometry case. Comparing the appropriate unit vectors from column groups two and four indicates how the constant-chord-length assumption affects the orientation of the associated planes.

As can be expected from the bending results for the SR-7L blade, the apparent total twist angle is also influenced by the slip effect. This follows from comparing group one and two results in table IV. Some of this effect is also evident in table V for the F7 blade. If one considers now twist angles in all the planes given in the tables and takes into consideration all blades, the plane perpendicular to the pitch axes appears to give the least error (in almost all cases) associated with laser

TABLE IV.—ABSOLUTE TWIST—STATIC TEST, SR-7L BLADE

(a) Blade angle $\beta = 22°$

Span position	Twist angle	True predicted $\bar\theta$, deg	$\hat{\bar n}$ $\hat i$	$\hat j$	$\hat k$	Predicted with slip θ, deg	$\hat n$ $\hat i$	$\hat j$	$\hat k$	Experimental (relative to reference point) $\tilde\theta$, deg	$\hat{\tilde n}$ $\hat i$	$\hat j$	$\hat k$	Predicted with slip and constant chord θ'', deg	$\hat n''$ $\hat i$	$\hat j$	$\hat k$
1	θ_{n_c}	0.9283	0.0604	−0.3906	0.9186	0.8506	−0.0238	−0.1584	0.9871	1.5324	−0.1665	0.2714	0.9479	0.8933	−0.0610	−0.0508	0.9968
	$\theta_{n_{ct}}$	.5925	−.2103	.4151	.8851	.6915	−.2103	.4151	.8851	1.5121	−.2103	.4151	.8851	.7808	−.2103	.4151	.8851
	θ_{n_h}	.6646	−.1771	.3248	.9290	.7424	−.1774	.3188	.9311	1.5305	−.1797	.3161	.9315	.8234	−.1787	.3209	.9301
	θ_k	.8571	0	0	1.0000	.8441	0	0	1.0000	1.4616	0	0	1.0000	.8953	0	0	1.0000
2	θ_{n_c}	0.3408	0.3859	−0.9224	0.0139	0.9732	0.3853	−0.9221	0.0352	0.8050	0.2561	−0.6416	0.7231	0.9332	0.3827	−0.9185	0.0997
	$\theta_{n_{ct}}$	−.1466	−.1841	.4028	.8966	−.3998	−.1841	.4028	.8966	.2759	−.1841	.4028	.8966	−.3276	−.1841	.4028	.8966
	θ_{n_h}	−.0322	−.0537	.0950	.9940	−.0824	−.0530	.1076	.9928	.5128	−.0550	.1044	.9930	−.0204	−.0539	.1090	.9926
	θ_k	.0047	0	0	1.0000	.0343	0	0	1.0000	.5822	0	0	1.0000	.0931	0	0	1.0000
3	θ_{n_c}	0.3709	0.0087	−0.0595	0.9982	1.0706	0.4621	−0.8296	0.3134	0.8584	0.3353	−0.6232	0.7065	1.0573	0.4650	−0.8341	0.2967
	$\theta_{n_{ct}}$	.2615	.3558	−.6576	.6641	.9829	.3558	−.6576	.6641	.8570	.3558	−.6576	.6641	.9632	.3558	−.6576	.6641
	θ_{n_h}	.3701	.0399	−.1147	.9926	.4416	.0409	−.0989	.9943	.6705	.0401	−.1053	.9936	.4195	.0410	−.0992	.9942
	θ_k	.3704	0	0	1.0000	.3355	0	0	1.0000	.6066	0	0	1.0000	.3138	0	0	1.0000

(b) Blade angle $\beta = 32°$

Span position	Twist angle	$\bar\theta$, deg	$\hat i$	$\hat j$	$\hat k$	θ, deg	$\hat i$	$\hat j$	$\hat k$	$\tilde\theta$, deg	$\hat i$	$\hat j$	$\hat k$	θ'', deg	$\hat i$	$\hat j$	$\hat k$
1	θ_{n_c}	1.4371	−0.0398	−0.0391	0.9984	1.5836	−0.3028	0.4303	0.8504	1.8663	−0.1928	0.2294	0.9540	1.9147	−0.2888	0.4041	0.8679
	$\theta_{n_{ct}}$	1.3458	−.2135	.2666	.9399	1.5497	−.2135	.2666	.9399	1.8645	−.2130	.2657	.9402	1.8862	−.2135	.2666	.9399
	θ_{n_h}	1.3785	−.1770	.2085	.9619	1.5160	−.1770	.1928	.9651	1.8650	−.1757	.1976	.9644	1.8516	−.1777	.1938	.9648
	θ_k	1.4390	0	0	1.0000	1.3518	0	0	1.0000	1.7867	0	0	1.0000	1.6683	0	0	1.0000
3	θ_{n_c}	0.5012	−0.0739	0.0625	0.9953	0.5343	0.3324	−0.4000	0.8541	0.7430	0.2245	−0.2780	0.9340	0.5224	0.3257	−0.3924	0.8602
	$\theta_{n_{ct}}$	.3768	.3753	−.4481	.8114	.5327	.3753	−.4481	.8114	.7172	.3781	−.4513	.8083	.5203	.3753	−.4481	.8114
	θ_{n_h}	.4943	.0346	−.0629	.9974	.4742	.0350	−.0591	.9976	.7104	.0352	−.0597	.9976	.4665	.0353	−.0595	.9976
	θ_k	.4989	0	0	1.0000	.4565	0	0	1.0000	.6940	0	0	1.0000	.4494	0	0	1.0000

(c) Blade angle $\beta = 25.8°$

Span position	Twist angle	$\bar\theta$, deg	$\hat i$	$\hat j$	$\hat k$	θ, deg	$\hat i$	$\hat j$	$\hat k$	$\tilde\theta$, deg	$\hat i$	$\hat j$	$\hat k$	θ'', deg	$\hat i$	$\hat j$	$\hat k$
1	θ_{n_c}	1.0429	0.0509	−0.2789	0.9590	0.9831	−0.1490	0.2068	0.9670	2.1918	−0.2079	0.3595	0.9097	1.2282	−0.1744	0.2718	0.9464
	$\theta_{n_{ct}}$	.7802	−.2145	.3769	.9011	.9646	−.2145	.3769	.9011	2.1914	−.2145	.3769	.9011	1.2192	−.2145	.3769	.9011
	θ_{n_h}	.8443	−.1773	.2942	.9392	.9796	−.1774	.2818	.9429	2.1830	−.1798	.2810	.9427	1.2281	−.1789	.2841	.9419
	θ_k	1.0036	0	0	1.0000	.9545	0	0	1.0000	2.0035	0	0	1.0000	1.1673	0	0	1.0000
2	θ_{n_c}	0.3797	0.3752	−0.7796	0.5015	0.9280	0.4275	−0.8767	0.2203	1.1493	0.1794	−0.3943	0.9013	0.9082	0.4191	−0.8618	0.2858
	$\theta_{n_{ct}}$	.0383	−.1934	.3637	.9112	−.1863	−.1933	.3637	.9112	.7393	−.1933	.3637	.9112	−.1217	−.1933	.3637	.9112
	θ_{n_h}	.1557	−.0554	.0872	.9946	.1025	−.0546	.0972	.9938	.9749	−.0566	.0948	.9939	.1599	−.0555	.0983	.9936
	θ_k	.1904	0	0	1.0000	.2045	0	0	1.0000	1.0359	0	0	1.0000	.2596	0	0	1.0000
3	θ_{n_c}	0.6009	−0.0264	0.0001	0.9996	1.1686	0.4707	−0.7473	0.4689	1.1874	0.2842	−0.4736	0.8336	1.1468	0.4776	−0.7570	0.4459
	$\theta_{n_{ct}}$	.4111	.3776	−.6124	.6945	1.1232	.3776	−.6124	.6945	1.1593	.3776	−.6124	.6945	1.0937	.3776	−.6124	.6945
	θ_{n_h}	.5969	.0354	−.0964	.9947	.6372	.0367	−.0815	.9960	1.0464	.0358	−.0870	.9956	.6004	.0367	−.0817	.9956
	θ_k	.6010	0	0	1.0000	.5481	0	0	1.0000	.9901	0	0	1.0000	.5115	0	0	1.0000

TABLE V.—ABSOLUTE TWIST—HIGH-SPEED TEST

Blade	Twist angle	True predicted				Predicted with slip				Experimental (relative to reference point)				Predicted with slip and constant chord			
		$\bar{\theta}$, deg	$\hat{\bar{n}}$			θ, deg	$\hat{n}$			$\tilde{\theta}$, deg	$\hat{\tilde{n}}$			θ'', deg	$\hat{n}''$		
			$\hat{i}$	$\hat{j}$	$\hat{k}$		$\hat{i}$	$\hat{j}$	$\hat{k}$		$\hat{i}$	$\hat{j}$	$\hat{k}$		$\hat{i}$	$\hat{j}$	$\hat{k}$
F11	θ_{n_c}	2.6149	−0.2457	0.0788	0.9661	2.6305	−0.3904	0.2027	0.8980	2.1629	−0.4619	0.2661	0.8461	2.6869	−0.3786	0.1923	0.9054
	$\theta_{n_{ct}}$	2.5955	−.1533	.0023	.9882	2.4932	−.1533	.0023	.9882	1.9623	−.1533	.0023	.9882	2.5612	−.1533	.0023	.9882
	θ_{n_h}	2.5857	−.1342	−.0176	.9908	2.4652	−.1338	−.0239	.9907	1.9327	−.1339	−.0244	.9907	2.5331	−.1330	−.0243	.9908
	θ_k	2.5519	0	0	1.0000	2.3884	0	0	1.0000	1.8502	0	0	1.0000	2.4594	0	0	1.0000
F1	θ_{n_c}	2.8421	−0.2026	0.1766	0.9632	2.8783	−0.2986	0.2718	0.9148	4.2322	−0.2655	0.2390	0.9340	2.8447	−0.2904	0.2637	0.9198
	$\theta_{n_{ct}}$	2.8186	−.1129	.0883	.9897	2.7723	−.1129	.0883	.9897	4.1286	−.1129	.0883	.9897	2.7493	−.1129	.0883	.9897
	θ_{n_h}	2.8052	−.0927	.0627	.9937	2.7421	−.0926	.0575	.9940	4.0930	−.0936	.0560	.9940	2.7197	−.0915	.0569	.9942
	θ_k	2.7390	0	0	1.0000	2.6351	0	0	1.0000	3.9565	0	0	1.0000	2.6185	0	0	1.0000
F7	θ_{n_c}	1.3597	−0.3882	0.3127	0.8669	1.6552	−0.6060	0.5028	0.6164	4.3063	−0.3623	0.2903	0.8857	1.7790	−0.5558	0.4585	0.6935
	$\theta_{n_{ct}}$	1.2522	−.1019	.0669	.9925	1.1706	−.1019	.0669	.9925	4.0292	−.1019	.0669	.9925	1.3799	−.1019	.0669	.9925
	θ_{n_h}	1.2398	−.0879	.0485	.9949	1.1374	−.0877	.0408	.9953	3.9855	−.0906	.0386	.9951	1.3461	−.0862	.0402	.9955
	θ_k	1.1792	0	0	1.0000	1.0210	0	0	1.0000	3.8186	0	0	1.0000	1.2346	0	0	1.0000

TABLE VI.—RELATIVE TWIST—STATIC TEST, SR-7L BLADE

(a) Blade angle $\beta = 22°$

Span position	Twist angle	True predicted $\bar{\theta}$, deg	$\hat{\bar{n}}$ $\hat{i}$	$\hat{j}$	$\hat{k}$	Predicted with slip θ, deg	$\hat{n}$ $\hat{i}$	$\hat{j}$	$\hat{k}$	Experimental (relative to reference point) $\tilde{\theta}$, deg	$\hat{\tilde{n}}$ $\hat{i}$	$\hat{j}$	$\hat{k}$	Predicted with slip and constant chord θ'', deg	$\hat{n}''$ $\hat{i}$	$\hat{j}$	$\hat{k}$
1	θ_{n_c}	0.8985	−0.1696	0.3193	0.9323	1.0062	−0.2315	0.5246	0.8193	1.6630	−0.2140	0.4463	0.8689	1.1037	−0.2416	0.5593	0.7930
	$\theta_{n_{ct}}$	.8931	−.1991	.4151	.8877	.9972	−.1989	.4151	.8878	1.6619	−.2047	.4151	.8864	1.0862	−.1989	.4151	.8878
	θ_{n_h}	.8985	−.1771	.3248	.9290	.9771	−.1774	.3188	.9311	1.6447	−.1797	.3161	.9315	1.0598	−.1787	.3209	.9301
	θ_k	.8413	0	0	1.0000	.8280	0	0	1.0000	1.4533	0	0	1.0000	.8792	0	0	1.0000
2	θ_{n_c}	0.9352	−0.3860	0.9225	0.0023	0.3599	−0.3840	0.9191	0.0885	0.8023	−0.2648	0.6392	0.7220	0.4126	−0.3751	0.9005	0.2197
	$\theta_{n_{ct}}$	.4081	−.1624	.4028	.9008	.1843	−.1645	.4028	.9009	.7632	−.1652	.4028	.9002	.2563	−.1614	.4028	.9009
	θ_{n_h}	.1035	−.0537	.0950	.9940	.0746	−.0530	.1076	.9928	.6405	−.0550	.1044	.9930	.1388	−.0539	.1090	.9926
	θ_k	.0022	0	0	1.0000	.0319	0	0	1.0000	.5793	0	0	1.0000	.0907	0	0	1.0000
3	θ_{n_c}	0.5694	−0.3854	0.6626	0.6422	0.6626	0.4208	−0.7572	0.4996	0.9540	0.3664	−0.6778	0.6374	0.6458	0.4268	−0.7672	0.4789
	$\theta_{n_{ct}}$	−.0859	.3619	−.6575	.6608	.6495	.3617	−.6575	.6609	.9534	.3541	−.6575	.6650	.6299	.3617	−.6576	.6609
	θ_{n_h}	.3109	.0399	−.1147	.9926	.3901	.0409	−.0989	.9943	.6864	.0401	−.1053	.9936	.3679	.0410	−.0992	.9942
	θ_k	.3658	0	0	1.0000	.3310	0	0	1.0000	.6083	0	0	1.0000	.3093	0	0	1.0000

(b) Blade angle $\beta = 32°$

Span position	Twist angle	$\bar{\theta}$, deg	$\hat{i}$	$\hat{j}$	$\hat{k}$	θ, deg	$\hat{i}$	$\hat{j}$	$\hat{k}$	$\tilde{\theta}$, deg	$\hat{i}$	$\hat{j}$	$\hat{k}$	θ'', deg	$\hat{i}$	$\hat{j}$	$\hat{k}$
1	θ_{n_c}	1.5608	0.1300	−0.3420	0.9301	1.4086	−0.1764	0.1833	0.9671	1.8910	−0.2119	0.2666	0.9402	1.7436	−0.1859	0.2003	0.9619
	$\theta_{n_{ct}}$	1.1741	−.2238	.2666	.9375	1.4016	−.2226	.2666	.9377	1.8910	−.2114	.2657	.9406	1.7380	−.2226	.2666	.9377
	θ_{n_h}	1.2501	−.1770	.2085	.9619	1.4085	−.1770	.1928	.9651	1.8848	−.1757	.1976	.9644	1.7435	−.1770	.1938	.9648
	θ_k	1.4576	0	0	1.0000	1.3681	0	0	1.0000	1.7841	0	0	1.0000	1.6846	0	0	1.0000
3	θ_{n_c}	0.4998	0.0024	−0.0266	0.9996	0.5668	0.3792	−0.4537	0.8065	0.8410	0.3566	−0.4316	0.8286	0.5544	0.3742	−0.4482	0.8119
	$\theta_{n_{ct}}$	.4120	.3742	−.4481	.8119	.5668	.3742	−.4481	.8119	.8405	.3743	−.4513	.8101	.5544	.3742	−.4481	.8119
	θ_{n_h}	.4992	.0346	−.0629	.9974	.4788	.0350	−.0591	.9976	.7274	.0352	−.0597	.9976	.4711	.0353	−.0595	.9976
	θ_k	.4997	0	0	1.0000	.4572	0	0	1.0000	.6970	0	0	1.0000	.4502	0	0	1.0000

(c) Blade angle $\beta = 25.8°$

Span position	Twist angle	$\bar{\theta}$, deg	$\hat{i}$	$\hat{j}$	$\hat{k}$	θ, deg	$\hat{i}$	$\hat{j}$	$\hat{k}$	$\tilde{\theta}$, deg	$\hat{i}$	$\hat{j}$	$\hat{k}$	θ'', deg	$\hat{i}$	$\hat{j}$	$\hat{k}$
1	θ_{n_c}	1.0124	0.0079	−0.1726	0.9850	1.0400	−0.2051	0.3605	0.9099	2.1842	−0.2055	0.3522	0.9131	1.2945	−0.2166	0.3907	0.8947
	$\theta_{n_{ct}}$	.8315	−.2124	.3769	.9016	1.0398	−.2113	.3769	.9018	2.1832	−.2148	.3769	.9010	1.2943	−.2113	.3769	.9018
	θ_{n_h}	.8837	−.1773	.2943	.9391	1.0358	−.1774	.2818	.9429	2.1769	−.1797	.2810	.9427	1.2847	−.1789	.2841	.9419
	θ_k	1.0005	0	0	1.0000	.9499	0	0	1.0000	2.0040	0	0	1.0000	1.1628	0	0	1.0000
2	θ_{n_c}	0.9001	−0.4301	0.8782	0.2091	0.4122	−0.3809	0.7834	0.4911	1.2480	−0.2423	0.5053	0.8282	0.4706	−0.3654	0.7530	0.5472
	$\theta_{n_{ct}}$	.5263	−.1719	.3637	.9155	.3296	−.1709	.3637	.9157	1.2277	−.1721	.3637	.9155	.3941	−.1709	.3637	.9157
	θ_{n_h}	.2776	−.0554	.0872	.9946	.2411	−.0546	.0972	.9938	1.1043	−.0566	.0948	.9939	.3003	−.0555	.0983	.9936
	θ_k	.1882	0	0	1.0000	.2024	0	0	1.0000	1.0336	0	0	1.0000	.2576	0	0	1.0000
3	θ_{n_c}	0.6715	−0.2611	0.3762	0.8890	0.9179	0.4286	−0.6816	0.5930	1.4274	0.3722	−0.6123	0.6976	0.8920	0.4381	−0.6957	0.5692
	$\theta_{n_{ct}}$	.1915	.3819	−.6124	.6921	.9102	.3818	−.6124	.6922	1.4274	.3723	−.6124	.6974	.8807	.3818	−.6124	.6922
	θ_{n_h}	.5633	.0354	−.0964	.9947	.6076	.0367	−.0815	.9960	1.0864	.0358	−.0870	.9956	.5708	.0367	−.0817	.9960
	θ_k	.5972	0	0	1.0000	.5444	0	0	1.0000	.9961	0	0	1.0000	.5078	0	0	1.0000

TABLE VII.—RELATIVE TWIST—HIGH-SPEED TEST

Blade	Twist angle	True predicted				Predicted with slip				Experimental (relative to reference point)				Predicted with slip and constant chord			
		$\bar{\theta}$, deg	$\hat{\bar{n}}$			θ, deg	$\hat{n}$			$\tilde{\theta}$, deg	$\hat{\tilde{n}}$			θ'', deg	$\hat{n}''$		
			$\hat{i}$	$\hat{j}$	$\hat{k}$		$\hat{i}$	$\hat{j}$	$\hat{k}$		$\hat{i}$	$\hat{j}$	$\hat{k}$		$\hat{i}$	$\hat{j}$	$\hat{k}$
F11	θ_{n_c}	2.6582	0.0010	−0.1395	0.9902	2.4978	−0.1572	−0.0138	0.9875	1.9704	−0.1388	−0.0313	0.9898	2.5661	−0.1494	−0.0201	0.9886
	$\theta_{n_{ct}}$	2.5898	−.1771	.0023	.9842	2.4970	−.1768	.0023	.9842	1.9676	−.1799	.0023	.9837	2.5645	−.1768	.0023	.9842
	θ_{n_h}	2.6147	−.1342	−.0176	.9908	2.4971	−.1338	−.0239	.9907	1.9705	−.1339	−.0244	.9907	2.5659	−.1330	−.0243	.9908
	θ_k	2.6630	0	0	1.0000	2.4977	0	0	1.0000	1.9755	0	0	1.0000	2.5688	0	0	1.0000
F1	θ_{n_c}	2.7584	−0.0044	−0.0385	0.9992	2.6742	−0.1110	0.0662	0.9916	4.0079	−0.1084	0.0585	0.9924	2.6524	−0.0993	0.0547	0.9936
	$\theta_{n_{ct}}$	2.7132	−.1334	.0883	.9871	2.6729	−.1333	.0883	.9871	4.0042	−.1385	.0883	.9864	2.6493	−.1333	.0833	.9871
	θ_{n_h}	2.7336	−.0927	.0627	.9937	2.6738	−.0926	.0575	.9940	4.0078	−.0936	.0560	.9940	2.6524	−.0915	.0569	.9942
	θ_k	2.7588	0	0	1.0000	2.6548	0	0	1.0000	3.9833	0	0	1.0000	2.6382	0	0	1.0000
F7	θ_{n_c}	1.3488	0.3064	−0.3039	0.9021	1.0599	−0.0649	0.0067	0.9979	3.8882	−0.1019	0.0297	0.9943	1.2724	−0.0451	−0.0101	0.9989
	$\theta_{n_{ct}}$	1.1194	−.1355	.0669	.9885	1.0553	−.1352	.0669	.9886	3.8817	−.1453	.0669	.9871	1.2634	−.1352	.0669	.9886
	θ_{n_h}	1.1545	−.0879	.0485	.9949	1.0592	−.0877	.0409	.9953	3.8886	−.0906	.0386	.9951	1.2698	−.0862	.0402	.9955
	θ_k	1.2180	0	0	1.0000	1.0592	0	0	1.0000	3.8747	0	0	1.0000	1.2728	0	0	1.0000

beam slip. Considering all blades, one can state that the slip effect produces an error of less than 0.2° in this plane. (Note that during the laser beam alignment an attempt was made to orient the beam in the plane perpendicular to pitch axes, but no uniform way of alignment could be applied for all blades.) Therefore the plane perpendicular to the pitch axis is considered the optimum plane for the twist angle, and all the subsequent results, unless noted otherwise, are for this plane.

Comparing group two and four results in tables IV and V shows that the maximum error associated with an apparent blade-chord-length change is about 0.3° (for SR–7L blade, $\beta = 32°$, span 1). This error can also be calculated from equation (42), derived under the planar geometry approximation. The result is usually within a few hundredths of a degree from the one derived from tables IV and V. It turns out, however, that if one considers, in addition, the error discussed in the previous paragraph, the resulting maximum error is actually only 0.23°. Thus it can be stated that the total systematic error associated with measured twist angle in a plane perpendicular to the pitch axis is less than a quarter of a degree for all blades and all measurement stations. This error is of about the same magnitude as the maximum experimental error, which is largely associated with the measurement of a laser beam incidence angle.

If desired, the measured twist angles can be corrected for these two systematic errors. The correction is more accurate the closer the predicted and experimental twist angles are. However, even a rough estimate can considerably reduce these errors. For example, even for a 50 percent error in estimating this correction, in the present case, the total systematic measurement error would be reduced to one eighth of a degree. In the plots presented in this report the measured twist angles include corrected points (square symbols) so that the effect of correction can be evaluated. As already mentioned, the plots for the SR–7L blade (i.e., static test data) were adjusted for this blade's excessively high reference speed. The plots of measured twist angles in figures 11 and 12 also include the true predicted absolute twist $\bar{\theta}_k$ at the design (or maximum) speed.

The relative twist angle results are presented in tables VI and VII. Although there are significant differences between relative and absolute twist angles, for the plane perpendicular to the pitch axis they are very small. In view of this, the relative twist angles were not plotted.

Note that for the high-speed test results (figs. 10 and 12), the first two points beyond the reference point (which is close to the origin of the axes) correspond to windmill conditions. Hence deflections for these points are attributed to centrifugal forces.

In general, the agreement between predicted and experimental twist angles, taking into account all blades (figs. 11 and 12), is not very good. Therefore, one cannot expect good agreement for both leading- and trailing-edge displacements normal to the chord (figs. 9 and 10). However, with the

exception of the results for $\beta = 32°$, which corresponds to the highest incidence condition, the agreement between predicted and experimental leading-edge displacements is fair for both series of tests. For a simplified planar model of blade section deflection, it therefore appears convenient to associate bending with the leading-edge displacement normal to the chord.

Before concluding this section, results for the F21 blade, presented in figure 13, will be discussed. These results are significant because the deflections for this blade are the largest and the agreement between predicted and measured twist angles is the best.

For this blade the manufacturer did not supply the complete finite-element outputs, but rather only the blade sections (deflected and undeflected) associated with the plane defined by the unit vector $\hat{n}_{cl}$. Thus the true deflections ($\bar{\theta}$ and $\bar{h}$) and the slip-effect corrections could not be evaluated. (This is why the results for this blade were not included in the tables.) Predicted results in figure 13 are therefore θ_k and h_p, and corrected twist includes only the chord correction effect. However, on the basis of the previous results the good agreement between predicted and measured deflections demonstrated in figure 13 would likely prevail for true predicted deflections. The test conditions for the F21 blade were close to the nominal design conditions: $N_f = 8085$ rpm, Mach 0.8, and $\beta = 61.8°$. The leading- and trailing-edge Z coordinates corresponding to laser beam tangency points were 29.50 and 29.68 cm.

## Computation of Twist Angle From Transit Measurements

During the static test of the SR–7L rotor the blade tip deflections were also measured on a transit rig available at the facility (ref. 11). These measurements were performed in the plane perpendicular to the pitch axis and at about the same blade tip span as the laser measurements. The transit was mounted in a horizontal plane on two perpendicular rails below the floor of the test section. The line of sight extended vertically upward, and the strobe light was timed so that the measured blade appeared to be in the horizontal position (i.e., its pitch axis was perpendicular to the line of sight). The axial blade deflections were measured relative to the static position by aligning the line of sight with a blade's leading and trailing edges and measuring the differential displacement of the transit carriage along the axial rail. The blades were therefore cut by the line of sight somewhat differently than by the laser beam, and hence each measurement must be compared independently with the predicted results. These data were supplied to the author by Hamilton Standard.

Because computing the twist angle involves the difference in the projected chord lengths between the deflected- and undeflected-blade sections, a correction term must be applied to account for the deformation effects other than twist, as for the laser measurements. The twist angle is given by the following equation:
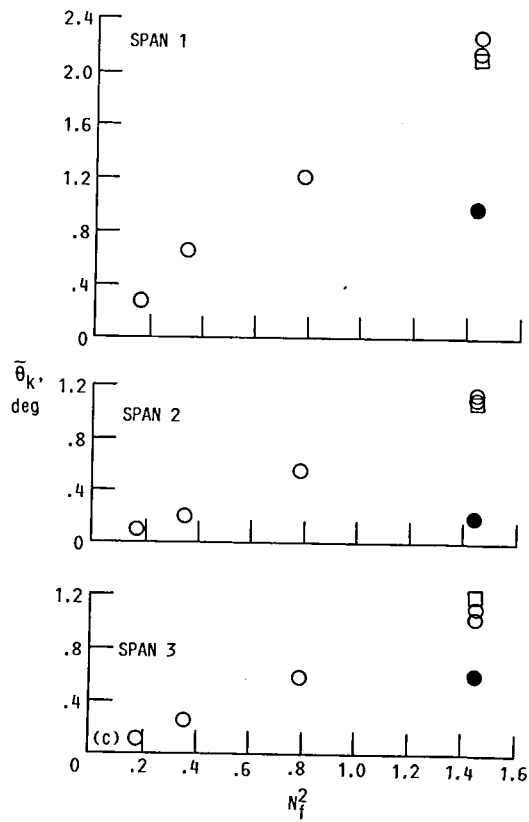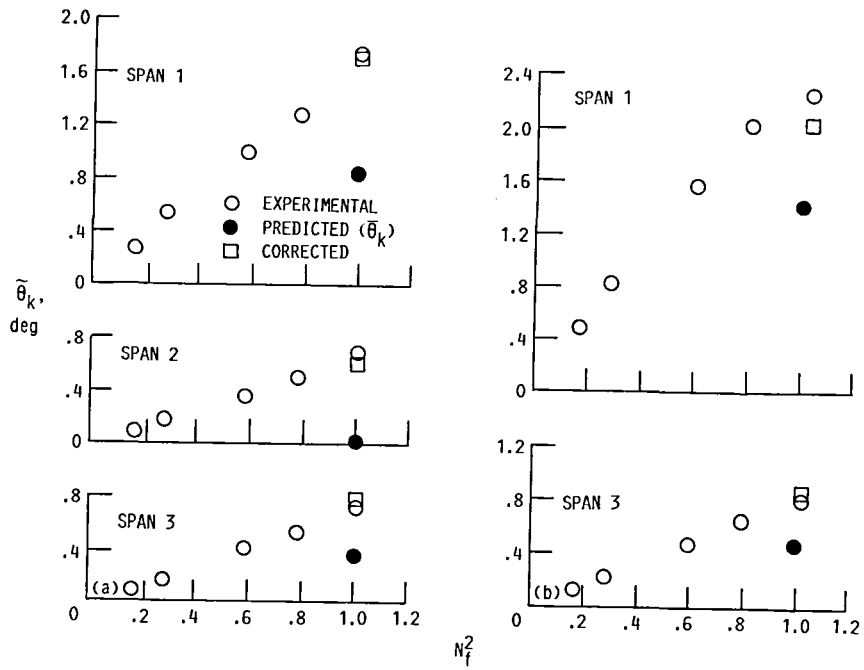
(a) Blade angle $\beta = 22°$.
(b) Blade angle $\beta = 32°$.
(c) Blade angle $\beta = 25.8°$.

Figure 11.—Absolute twist—SR–7L blade, static test.
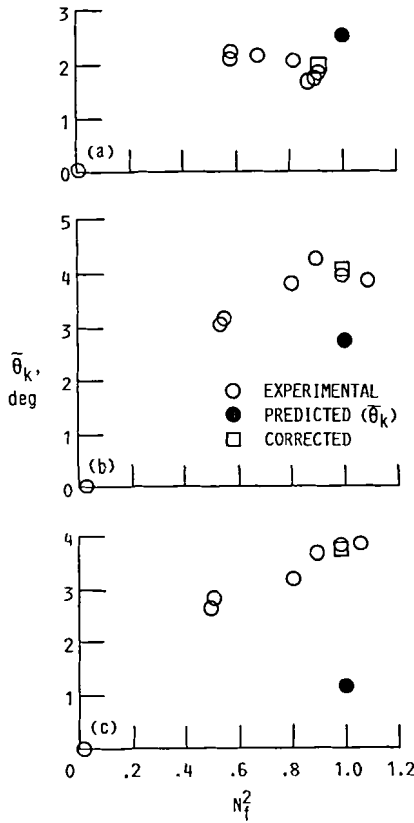
(a) F11 blade.
(b) F1 blade.
(c) F7 blade.

Figure 12.—Absolute twist—high-speed test.

$$2C_k \sin\left(\frac{\theta}{2}\right) = \frac{(\delta_y)_{TE} - (\delta_y)_{LE}}{\cos \beta_k}$$

$$+ (C_k' - C_k)\left(\tan \beta_k + \sin \frac{\theta}{2}\right) \qquad (82)$$

where δ_y denotes axial deflection. Since usually $\theta/2 \ll \beta_k$, this equation can be simplified to

$$\theta \sim \frac{(\delta_y)_{TE} - (\delta_y)_{LE}}{C_k \cos \beta_k} + \frac{(C_k' - C_k)}{C_k} \tan \beta_k \qquad (83)$$

The correction term associated with the constant-chord assumption is the last term in equation (83). This term now involves the tangent of β_k rather than $\gamma + \theta/2$, and hence it is expected to be more significant for the transit measurements than for the laser measurements.

As an example, the twist angle for $\beta = 25.8°$ computed from transit measurements is presented in figure 13. The deflections were actually computed relative to the $N_f = 0.17$ point, for
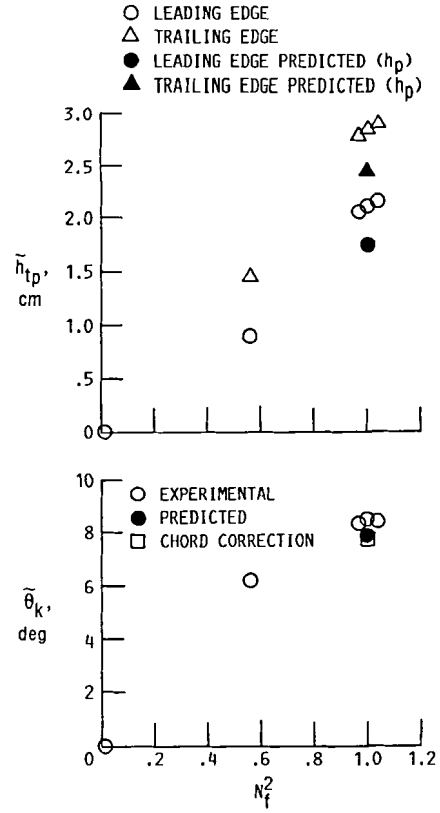

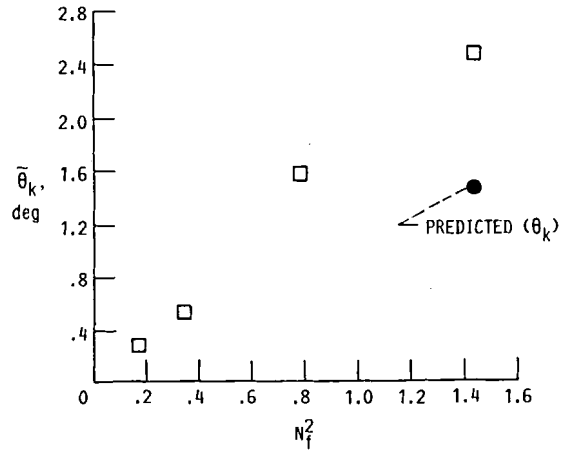Figure 13.—Bending and twist deflections—F21 blade.

Figure 14.—Corrected absolute twist for SR-7L blade—transit data, blade angle $\beta = 25.8°$.

which the twist angle was taken to be the same as in figure 11(c) for laser measurements (since absolute deflections relative to the static blade position may include some free-play effect). Some unsteadiness was reported for the $N_f = 0.78$ point at the leading edge, and the axial deflection there corresponds to the average reading.

The measurement plane is given by $Z/Z_{max} = 0.967$. The true predicted twist was computed as for the laser data. The

measured twist includes constant-chord correction (0.51°) and slip correction (0.037°), both of which increased the twist angle. Corrections for other points were applied proportionately to the deflections.

The agreement between measured, corrected twist angles and the respective predicted twist angles in figure 14 is similar to that in figure 11(c) (span position 1) for laser measurements. In both figures measured values are considerably higher than predicted.

Concluding Remarks

Propeller blade deflections caused by centrifugal and aerodynamic loads were measured with a nonintrusive optical method that uses low-power helium-neon lasers. Complete results were obtained for four recently designed blade prototypes, one of which was measured at three spanwise positions and three blade angles. Measurements were made in a plane nearly perpendicular to the pitch axis. Twist angles and leading- and trailing-edge bending deflections were obtained by using one laser per spanwise station with a total systematic (and therefore correctable) error of less than one quarter of a degree. The experimental measurement error was estimated to be of about the same magnitude.

Systematic geometric errors are especially significant for stiff blades, for which deflections are small. For such blades appropriate definition of deflections associated with a particular plane (chosen to minimize these errors) is essential.

Predicted and experimental bending and twist deflections were compared for five blade prototypes. With the single exception of a high-incidence test on one of the blades, the agreement between predicted and experimental leading-edge bending deflections was generally fair. However, the agreement between corresponding twist angles was poor, except for one blade prototype for which it was very good.

Lewis Research Center
National Aeronautics and Space Administration
Cleveland, Ohio, May 10, 1988

References

1. Zablotskiy, I.E.; Korostelev, Y.A.; and Sviblov, L.B.: Contactless Measuring of Vibrations in the Rotor Blades of Turbines. Technical Translation, Foreign Technology Division, Wright-Patterson Air Force Base, OH, FTD-HT-23-673-74, 1974.
2. Nieberding, W.C.; and Pollack, J.L.: Optical Detection of Blade Flutter in YF-100 Turbofan Engine. ASME Paper 77-GT-66, Mar. 1977.
3. Roth, H.: Vibration Measurements of Turbomachine Rotor Blades With Optical Probes. Measurement Methods in Rotating Components of Turbomachinery, B. Lakshminarayana and P. Runstadler Jr., eds., ASME, 1980, pp. 215-224.
4. McCarty, P.E.; Thompson, J.W., Jr.; and Ballard, R.S.: Noninterference Technique for Measurement of Turbine Engine Compressor Blade Stress. J. Aircraft, vol. 19, no. 1, Jan. 1982, pp. 65-70.
5. Kurkov, A.P.: Measurements of Self-Excited Rotor-Blade Vibrations Using Optical Displacements. J. Eng. Gas Turbines Power, vol. 106, no. 1, Jan. 1984, pp. 44-49.
6. Kurkov, A.P.: Formulation of Blade-Flutter Spectral Analyses in Stationary Reference Frame. NASA TP-2296, 1984.
7. Lawrence, C.; and Meyn, E.H.: The Use of an Optical Data Acquisition Systems for Bladed Disk Vibration Analysis. Vibrations of Blades and Bladed Disk Assemblies, R.E. Kielb and N.F. Rieger, eds., ASME, 1985, pp. 65-73.
8. Stefko, G.L., et al.: Propeller Flow Visualization Technique. Flow Visualization and Laser Velocimetry for Wind Tunnels, NASA CP-2243, W.W. Hunter, Jr., and J.T., Foughner Jr., eds., 1982, pp. 75-89.
9. Srinivasan, A.V.; and Fulton, G.B.: Advanced Turboprop Vibratory Characteristics. (R84-956627-1, United Technologies Research Center; NASA Contract NAS3-23533) NASA CR-174708, 1984.
10. Srinivasan, A.V.; Kielb, R.E.; and Lawrence, C.: Dynamic Characteristic of an Assembly of Prop-Fan Blades. J. Eng. Gas Turbines Power, vol. 108, no. 2, Apr. 1986, pp. 306-312.
11. Taylor, L.M.: Sighting Devices for Propeller Blade Observation. Air Corps Technical Report 4160, Dec. 1935.
12. Stargardter, H.: Optical Determination of Rotating Fan Blade Deflections. J. Eng. Power, vol. 99, no. 2, Apr. 1977, pp. 204-209.
13. DeGeorge, C.L.; Turnberg, J.E.; and Wainauski, H.S.: Large Scale Advanced Prop-Fan (LAP) Static Rotor Test Report. (HSER-116227, Hamilton Standard Division; NASA Contract NAS3-23051) NASA CR-180848, 1987.
14. Sullivan, T.J.: Aerodynamic Performance of a Scale-Model, Counter-Rotating Unducted Fan. Advanced Technology for Aero Gas Turbine Components, AGARD CP-421, Paris, France, 1987, pp. 22-1—22-16.

1. Report No. NASA TP-2841	2. Government Accession No.	3. Recipient's Catalog No.
4. Title and Subtitle **Optical Measurement of Propeller Blade Deflections**		5. Report Date **September 1988**
		6. Performing Organization Code
7. Author(s) Anatole P. Kurkov		8. Performing Organization Report No. **E-4131**
		10. Work Unit No. **535-03-01**
9. Performing Organization Name and Address National Aeronautics and Space Administration Lewis Research Center Cleveland, Ohio 44135-3191		11. Contract or Grant No.
12. Sponsoring Agency Name and Address National Aeronautics and Space Administration Washington, D.C. 20546-0001		13. Type of Report and Period Covered **Technical Paper**
		14. Sponsoring Agency Code

15. Supplementary Notes

16. Abstract

A nonintrusive optical method for measuring propeller blade deflections is described and evaluated. The measurement does not depend on blade surface reflectivity. Deflection of a point at the leading edge and a point at the trailing edge in a plane nearly perpendicular to the pitch axis is obtained with a single light beam generated by a low-power, helium-neon laser. Quantitative analyses are performed from taped signals on a digital computer. Averaging techniques are employed to reduce random errors. Measured deflections from a static test and a series of high-speed tests are compared with available predicted deflections, which are also used to evaluate systematic errors.

17. Key Words (Suggested by Author(s)) Blade deflection Turboprop blades Propeller	18. Distribution Statement Unclassified – Unlimited Subject Category 35		
19. Security Classif. (of this report) Unclassified	20. Security Classif. (of this page) Unclassified	21. No of pages 32	22. Price* A03